Department of Physics and Astronomy

University of Heidelberg

Bachelor Thesis in Physics
submitted by

Roman Constantin Hector

born in Freudenstadt (Germany)

2022

Characterization of a Xenon-Recycling-System for an Extreme-Ultraviolet Frequency Comb

This Bachelor Thesis has been carried out by Roman Constantin Hector

at the

Max Planck Institute for Nuclear Physics in Heidelberg

under the supervision of

apl. Prof. José R. Crespo López-Urrutia

Abstract:

To perform precision spectroscopy of highly charged ions, an extreme-ultraviolet frequency comb has been developed at the Max-Planck-Institute for Nuclear Physics in Heidelberg. By generating high-harmonics in an enhancement cavity, the comb structure of a pulsed laser in the near-infrared spectrum is transferred to the extreme-ultraviolet spectrum, which necessitates the use of rare noble gases such as xenon. To reduce their consumption, a gas recycling system was designed and its functionality was investigated in this work. For this purpose, an automatic readout system was constructed, which allows reliable measurement of high pressures.
In addition, an alignment laser unit was assembled, which allows the orientation of deflecting and focusing mirrors in the beamline with the help of a counter-propagating optical laser necessary for spectroscopy, even before the generation of high harmonics.
The goal of the experimental setup is to realize spectroscopy with highly charged ions trapped in the cryogenic Paul trap of the CryPTEx SC system, which will be linked to the cavity with the beamline as a connection in the future.

Zusammenfassung:

Um Präzisionsspektroskopie an hochgeladenen Ionen durchzuführen, wurde ein extrem-ultravioletter Frequenzkamm am Max-Planck-Institut für Kernphysik in Heidelberg entwickelt. Mittels Erzeugung hoher Harmonischer in einer Verstärkungs-Kavität wird dabei die Kammstruktur eines gepulsten Lasers im nahen infrarot Spektrum auf das extrem-ultraviolette Spektrum übertragen, was die Nutzung seltener Edelgase wie Xenon notwendig macht. Um deren Verbrauch zu reduzieren, wurde ein Gas-Recycling System entworfen, dessen Funktionalität in dieser Arbeit untersucht wurde. Dafür wurde eine Ausleseautomatik konstruiert, mit der eine zuverlässige Messung hoher Drücke möglich ist.
Zusätzlich wurde eine Justier-Laser Einheit entwickelt, mit der die Ausrichtung von Umlenk- und Fokussier-Spiegel mit einem gegenläufigen optischen Laser in der für die Spektroskopie notwendigen Beamline noch vor der Erzeugung hoher Harmonischer möglich ist.
Ziel des experimentellen Aufbaus ist, Spektroskopie mit hochgeladenen Ionen zu ermöglichen, die in der kryogenen Paul-Falle des CryPTEx SC Systems gefangen werden, welche an die Kavität über die Beamline angeschlossen wird.

Contents

1 Introduction

Using resources is inevitably accompanied by the production of waste. No engine can run without the emission of heat, no plastics can be utilized without the eventual conversion of hydrocarbons into carbon dioxide and no industrial-sized cultivation of food gets by without the - albeit unintentional - dissipation of raw materials. Especially in a time where the finiteness of many resources becomes more apparent than ever before, with petroleum being perhaps one of the best examples, the efficient usage of the materials we work with grows into an imperative, not only in the ecological, but also in an economical sense. New ways of manufacturing commodities and more efficient handling of energy may play a role as important as overall reduction, and a third way of dealing with waste can also help minimizing the negative side effects the interaction with our environment brings with it: recycling. The process of recycling involves collecting unused waste products and its subsequent reassembly, chemical conversion, reshaping or extracting of valuable constituents for later utilization. Thus, many materials used by humans are suited for recycling: from the steel in heavy industry over plastic bottles to the electronic components in our phones.

Often times, recycling can also be applied to less visible substances, such as noble gases. Whereas argon makes up almost 1 % of Earth´s atmosphere, its heavier brothers are much rarer:

Table 1.1: Proportions of non-radioactive noble gases in the lower atmosphere of the earth in ppm by volume fraction [1].

Element	Abundance (ppm)
He	5.24
Ne	18.18
Ar	9340
Kr	1.14
Xe	0.09

Since these gases also have applications in industry (xenon-krypton headlights [2]), in space travel (ionic propulsion [3]) and in the production of semiconductor chips [4], recycling methods for noble gases are of interest because their extraction from air involves high energetic investments and are rather costly.

The scientific field also has purposes revolving around the use of heavier noble gases, such as experimental anesthetic agents in medicine [5]. Another example in

the realm of physics is frequency multiplication by the process of high-harmonic generation [6, 7] contributing to the advance of modern spectroscopy.

1.1 The importance of Spectroscopy

The development of methods in spectroscopy is a very important pillar of modern experimental physics, since a higher resolution of the observed energies emitted when transitions of quantum states occur, offers a more precise insight in the fundamental mechanics behind the phenomena presented by the matter in our universe. One technology used for characterizing these transitions that has become indispensable in modern spectroscopy, is the laser, especially in the configuration of a frequency comb (FC), allowing a very precise and absolute measurement of the frequencies to be observed. FCs have already been demonstrated in the mid-infrared [8] and the visible and near-infrared spectral range [9]. However, for large parts of the electromagnetic spectrum there are no conventional lasers with sufficient stability, coherency and a linewidth narrow enough available so far. As a means to combat this, the process of High Harmonic Generation (HHG) - which often involves heavy noble gases such as krypton or xenon - enables the transfer of precise, high end FCs in the infra-red (IR) part of the electromagnetic spectrum into the ultraviolet (UV) and extreme-ultraviolet (XUV) regime [10].

The potential for answers to some of the most important unresolved questions in modern physics motivates the development of these kinds of spectroscopy tools, giving rise to the XUV frequency comb [11].

1.2 The Search for Physics Beyond the Standard Model

Many laws, regularities and properties of particles in the quantum world are now known to a limit that was not imaginable a hundred years ago and General Relativity has been thoroughly tested over the course of the last century and even today, making for example the precise usage of the global positioning system (GPS) possible [12].
The theories describing the smallest and largest part of our universe (the Standard Model and General Relativity, respectively) correspond well to the experiments we can conduct. For example, the relative mass difference between the electron and its antiparticle proposed by Dirac in 1928 [13] is smaller than 8×10^{-9} (using a confidence interval of 90%) according to the particle data group (PDG). The masses of the electron and the positron should be equal according to the Standard Model. However, some big open questions still cannot be answered. One of these

mysteries is the apparent asymmetry between the amount of matter and antimatter in the observable parts of our universe. With our current understanding of the physical world, which includes some crucial laws of conservation, e.g. of the baryonic number, this asymmetry cannot be explained.

However, the processes that govern the events in the quantum world strictly depend on the fundamental constants involved [14], like the fine-structure constant α or the coupling constant for the strong nuclear force α_s. Even small variations over time of constants like these in varying processes or for different particles might give some important insight here [15]. Hence, it is critical to be able to measure them with high precision.

1.3 Time Measurement

Every measurement relies on an accurate definition of an according unit. This also applies when we want to determine values of certain frequencies in subatomic processes, which makes the knowledge of the exact time scaling enormously important. Nowadays, atomic clocks are commonly used, because their accuracy outmatches other types (like the quartz clock) by orders of magnitude [16].

Atomic clocks make use of the fact that transition frequencies of some atoms or ions are highly stable across time and show a very small fundamental uncertainty, rendering them appropriate for the definition of the units of time. Increasing the accuracy of atomic clocks, i.e. increasing the time until the clock is off the "real" time, requires working with higher and higher frequencies giving rise to the so-called optical atomic clocks utilizing the transitions in the optical part of the spectrum instead of radio- or microwave frequencies like conventional atomic clocks [17]. Currently, the second is defined as the duration of 9,192,631,770 periods of the transition radiation between the two hyperfine levels of the ground state of ^{133}Cs [18]. The usage of such frequencies requires a means of counting the numbers of oscillations, such that a point in time can be determined that marks the passing of one second. Moving to higher frequencies is key to increasing the accuracy of these clocks but makes counting the numbers of oscillations even harder.

A solution to this problem is given by the FC, which can be thought of as a ruler for frequencies allowing the absolute determination of their values with a small-scale tabletop device.

1.4 XUV Spectroscopy

The application of the FC in the UV and XUV spectrum not only advances the development of optical and nuclear clocks, it will also enable accurate spectroscopy

of highly charged ions (HCI). These ions, characterized by the lack of many electrons, have some rather interesting properties. Their transition frequencies often lie beyond the optical part of the electromagnetic spectrum reaching as far as into the X-ray regime. Since the electrons are moving much closer to the nucleus, the influence of external perturbations of the electric or magnetic field is greatly reduced compared to neutral atoms or singly charged ions. This allows for a much more precise determination of fundamental constants.

Combining the advantage of a FC, making absolute measurements of transition frequencies over a broad spectrum possible, with the HHG process, transferring the comb structure into the XUV-region, yields a method for examining the promising transitions HCIs exhibit.

In this work, a gas recycling system supporting the reduction of costly noble gases involved in the HHG process of a XUV FC is characterized and the development of a alignment laser system aiding the adjustment of optical elements inside a beamline is discussed.
This work is structured as follows: In the second chapter, an overview of the theoretical foundation revolving around the experiment is given. The third chapter deals with the experimental setup and the devices used for investigating the recycling system and the laser alignment system. Thereafter, an analysis is given on the efficiency of the recycling system.

2 Theory

In this section an overview is given on the theoretical fundamentals concerning the basic working principle of a FC and the application of this technology in the XUV regime via HHG as well as the thermodynamic processes and principles needed to understand the recycling pumping system for noble gases.

2.1 The Frequency Comb and High Harmonics Generation

2.1.1 Lasers and Spectroscopy

Electromagnetic spectroscopy with small ensembles of atoms or ions requires very stable and well controllable light sources combined with coherence times as long as possible. The reason for this is that the coherence time must be at least as long as the lifetime of the transition observed in order to trigger them effectively. Additionally, the bandwidth of the driving electric field is of great importance, when it comes to the efficiency of transition processes. Especially with small ensembles of atoms, the number of transitions must be maximized in order to get enough data-samples.

Following [19], we can calculate the dipole transition probability for a light source with the spectral energy density $\rho(\omega)$ given that the transition occurs at a sharply defined frequency ω_{ba}:

$$P_{ab}(t) = \frac{\vec{D}_{ab}^2}{2\epsilon_0\hbar^2} \int \rho(\omega) \left(\frac{sin(\omega_{ba} - \omega)t/2}{(\omega_{ba} - \omega)/2} \right)^2 d\omega, \tag{2.1}$$

with $\vec{D}_{ab}$ denoting the dipole matrix element.
This means that for the probability of a transition to be as big as possible, the spectral bandwidth of the source should be as small as possible with the center frequency matching the transition frequency. Here, lasers play an extremely important role, since their spectral bandwidth can be lower than 1Hz [20], allowing the overlap integral (see above) having a considerable size without the need for extremely large total source powers.

2.1.2 Pulsed Lasers

In the simplest case, a laser will show a continuous Sine-wave in the electric field component resulting in a strictly periodical temporal intensity profile, which is called a continuous wave (CW) laser. Using such a laser for spectroscopy introduces a certain problem: it can only be used for transitions of matching frequencies, especially if the laser has a narrow bandwidth. In order to circumvent this problem, a pulsed laser can be put into practise using two tunable and easily measurable frequencies in the radio-spectrum giving rise to a frequency comb that can be thought of as an absolute ruler for frequencies in the infra-red, visible or even UV regime. A second distinct advantage of pulsed lasers is the high peak intensities reached by the concentration of the delivered energies in very small time intervals that can be used for processes like HHG.

In order to build such a frequency comb, having a means of producing a highly stable pulsed laser is of utmost importance. As we will see, electronically switching a laser on and off is insufficient for this purpose for several reasons: For one, extracting a train of exactly equivalent gaussian pulses from a CW source is not easily done. Another key problem with the realization of a frequency comb in the optical and UV region is achieving the high repetition rate of many MHz, which is the reason why we cannot simply turn the laser on and of very rapidly. Moreover, it would be very preferable to store the energy in the time between the pulses, such that the peak intensity is as large as possible.

Although there are other techniques to circumvent this problem, such as Q-switching, only the method of mode-locking is discussed here, following [21] and [19].

Mode-Locking

Using mode-locking enables the realization of pulses in the ps range without electronically controlling an attenuator, and instead bringing all the possible modes of a laser in a fixed phase-relation.

To get an understanding of the working principle behind the mode-locking method, we imagine a laser with a single frequency ν_0, which would show the following intensity profile:

$$I = I_0 \ \cos^2(2\pi\nu_0 t). \tag{2.2}$$

For a laser cavity being able to support such a frequency, the length d has to match a multiple of half the carrier wavelength:

$$\nu_0 = n\frac{c}{2d}, \qquad n \in \mathbb{N}. \tag{2.3}$$

If a modulator is inserted, the transmitted intensity can be modified to the following profile:

$$I_t = I_0(1 + a\,\cos(2\pi f t))\cos^2(1\pi\nu_0 t). \tag{2.4}$$

Calculating the Fourier-transform of this distribution results in an interesting spectral profile:

$$\begin{aligned}\mathcal{F}\{I_t\} = I_t(w) = I_0\,\Big[&\sqrt{\frac{\pi}{8}}\,(\delta(\omega - 4\pi\nu_0) + \delta(\omega + 4\pi\nu_0) + 2\delta(\omega)) \\ &+ a\sqrt{\frac{\pi}{82}}(\delta(\omega - 4\pi\nu_0 - 2\pi f) + \delta(\omega - 4\pi\nu_0 + 2\pi f) \\ &+ \delta(\omega + 4\pi\nu_0 - 2\pi f) + \delta(\omega + 4\pi\nu_0 + 2\pi f) + 2\delta(\omega - 2\pi f) + 2\delta(\omega + 2\pi f))\Big].\end{aligned} \tag{2.5}$$

This means, the modulation results in the formation of sidebands right and left to the carrier frequency ν_0. If the frequencies of these sidebands correspond to the resonant frequency of the laser cavity, they also get amplified.

These new sideband-waves also get modified by the modulator and thus giving rise to infinitely many sidebands all spaced apart by the frequency f.

However, in a more realistic situation, the frequency interval, in which radiation is reasonably well amplified inside the laser cavity, is limited by the resonator gain bandwidth $\Delta\nu$. Thus, the number of supported modes N is also limited:

$$N = \frac{\Delta\nu}{c/2d}\ . \tag{2.6}$$

Assuming the bandwidth to be centered around ν_0, we can write the wave function as a symmetric superposition of harmonic oscillations:

$$A = \sum_{q=-m}^{m} A_q\,\cos(2\pi(\nu_0 + qf)t) \qquad \text{with } N = 2m + 1. \tag{2.7}$$

If all the amplitudes are assumed to be equal ($A_q = A_0$), the intensity can be simplified to

$$I_t \propto |A^2| = A_0^2\,\frac{\sin^2(\pi N f t)}{\sin^2(\pi f t)}\cos^2(2\pi\nu_0 t). \tag{2.8}$$

This distribution shows an underlying carrier wave with an envelope characterizing identical pulses spaced apart by a certain time. The pulse parameters can be

extracted from the intensity distribution:

$$\text{Pulse Distance: } T_{\text{rep}} = \frac{1}{f} \,, \tag{2.9}$$

$$\text{Pulse Width: } \tau_{\text{E}} = \frac{1}{N \cdot f} = \frac{1}{\Delta\nu} \,. \tag{2.10}$$

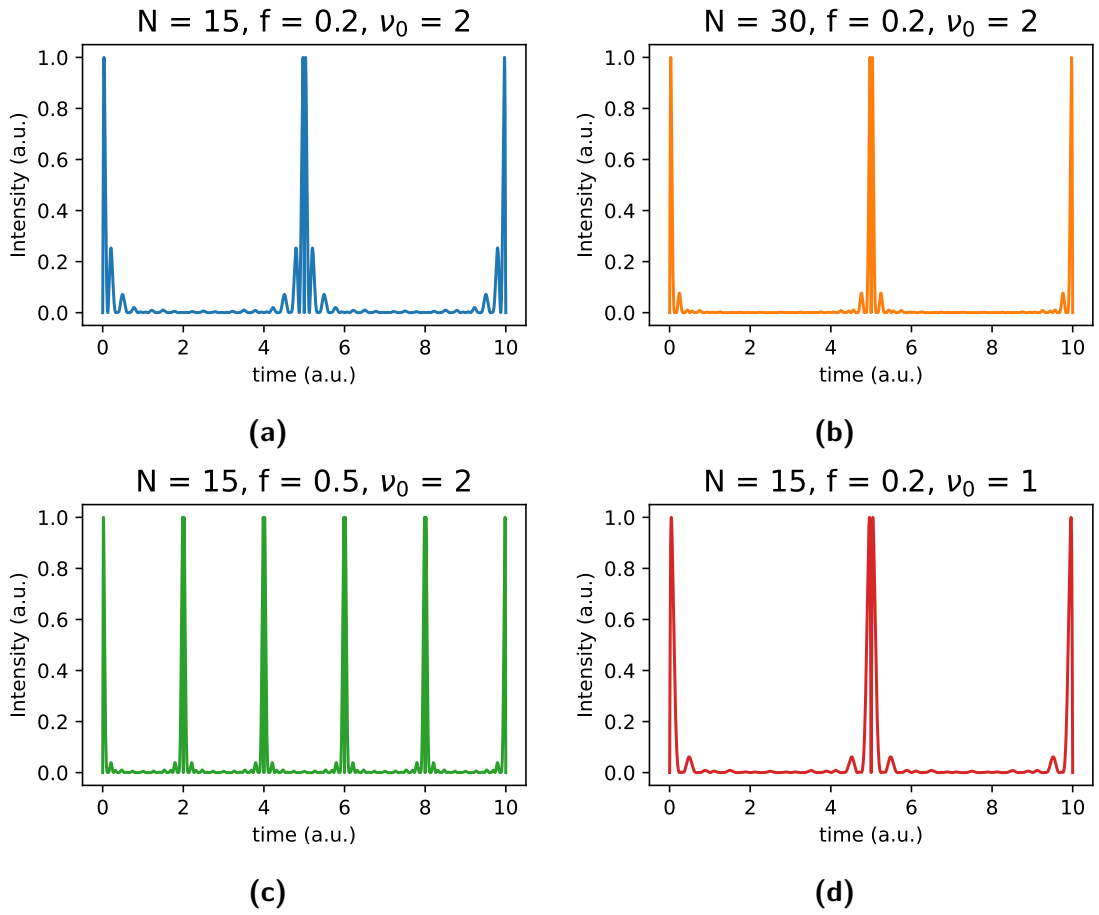

Figure 2.1: Temporal intensity profile of an idealized mode-locked laser for different parameters. An increase of supported sidebands (b) leads to narrower pulses and an increase of the modulation frequency (c) brings the pulses closer together. The center frequency also has an influence on the sidebands (d). The absolute peak intensities reached would be bigger with narrower pulses that are spaced far apart from each other, since the transported energy is released in very small intervals.

Fig. 2.1 shows the temporal profile of an ideal mode-locked pulsed laser. The characteristics of the single pulses as well as their temporal distance and consequently the maximum intensities reached by each pulse can be controlled via the gain bandwidth and the modulation frequency f.

Allowing for more different modes reduces the pulse width, which is often favourable, since more energy is concentrated in a shorter amount of time giving rise to larger bursts of power. However, the active bandwidth where resonance takes place must be maximized, since smaller modulation frequencies lead to an increase of the pulse width.

The repetition rate is equal to the modulation frequency and thus only depends on the modulator used. However, if the modulator can be externally controlled, the repetition rate might be varied to some extent.

Frequency Comb

Starting from a plane wave as a solution of Maxwell´s equation

$$\left(\Delta - \frac{1}{c^2}\partial_t^2\right)\vec{E} = \mu_0 \partial_t^2 \vec{P}, \tag{2.11}$$

the electric field in the z-direction in the frequency domain assuming a polarization $\vec{P} = 0$ (vacuum) is given by

$$E(\omega, z) = E(\omega, 0)e^{-ikz}. \tag{2.12}$$

This is a general form of a planar wave oscillating with the angular frequency ω with a wavelength of $\lambda = 2\pi/k$, with k being the wave number. The relation of the wave number and the angular frequency $k(\omega)$ is called the dispersion relation and governs, how a wave packet consisting of multiple frequencies behaves over time. In the special case of light propagating through vacuum, the speed of light is constant throughout the entire spectrum:

$$c_0(\omega) = \frac{\omega}{k(\omega)} = c. \tag{2.13}$$

Principally, there are multiple forms these pulses could take on, depending on the generation mechanism for different purposes, such like $sech^2$- or Lorentzian-shaped. Here, we focus on those characterized by a gaussian pulse shape. In the time-domain, such a Gaussian-shaped pulse defining the envelope of the electric field is given by

$$A_0(t) = E_0 e^{-2\ \ln 2\left(\frac{t}{\tau}\right)^2}, \tag{2.14}$$

where τ corresponds to the FWHM-width of the intensity profile $I(t) = |E(t)|^2$. We can write the electric field of a pulsed laser under continuous operation as a series of Gauss-shaped pulses spaced apart by the repetition time T_{rep} with the

underlying carrier wave of the frequency ω_c:

$$E_t(t) = e^{i\omega_c t} E_0 \sum_{q=0}^{N-1} e^{-\frac{2\ \ln 2}{\tau^2}(t-qT_{\mathrm{rep}})^2} = e^{i\omega_c t} A(t). \tag{2.15}$$

Introducing the carrier-to-envelope phase $\Delta\Phi_{CE}$, we can decouple the center frequency ω_c [22]:

$$E_{\mathrm{pt}}(t) = \sum_{q=0}^{N-1} A_0(t - qT_{\mathrm{rep}}) e^{i(\omega_c t - q(\omega_c T_{\mathrm{rep}} + \Delta\Phi_{\mathrm{CE}}))}. \tag{2.16}$$

The middle term in the exponent ($\exp(iq\omega_{\mathrm{c}}T_{\mathrm{rep}})$) centers the underlying oscillation to the according envelope to keep track of the phase shift with $\Delta\Phi_{\mathrm{CE}}$.

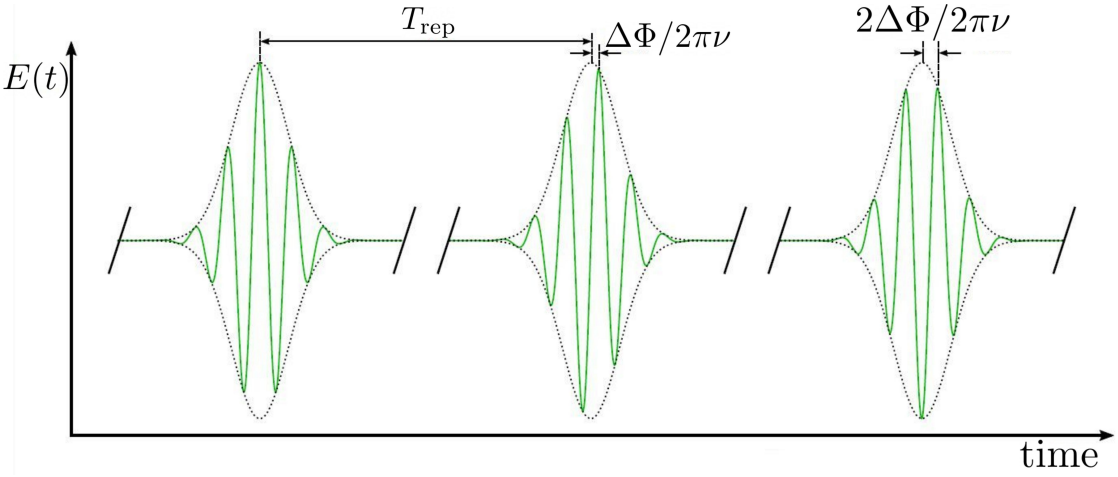

Figure 2.2: Illustration of the electric field over time. The carrier-phase of a neighbouring pulse is shifted relative to the envelope by $\Delta\Phi_{\mathsf{CE}}$. Adapted from [23] (modified).

Applying the Fourier-Transformation yields the spectrum of the electric field for such a pulse train:

$$\tilde{E}_{\mathrm{pt}}(\omega) = \sum_{q=0}^{N-1} e^{i(q(\Delta\Phi_{CE} - \omega_c T_{rep}) + \Phi_0)} \int A_0(t - qT_{rep}) e^{i[(\omega-\omega_c)t]} dt. \tag{2.17}$$

By using Poissons sum formula, we can reformulate Eqn. 2.17 for the case $N \to \infty$:

$$\tilde{E}_{\mathrm{pt}}(\omega) = e^{i\Phi_0} \tilde{\mathrm{A}}(\omega - \omega_c) \sum_{q=0}^{\infty} \delta(-\omega T_{rep} + \Delta\Phi_{CE} - q2\pi), \tag{2.18}$$

with $\tilde{A}(\omega)$ being the Fourier-Transform of the Gauss-shaped envelope $A_0(t)$: $\tilde{A}(\omega) = \int A_0(t)e^{-i\omega t}dt$.

In this form, it is clear that the electric field and thus the intensity only shows components at very well defined frequencies (δ-peaks) which are all equally spaced apart by the repetition rate. The additional global phase Φ_0 is not of interest here, since it does not occur in the intensity spectrum $\tilde{I}(\omega) \propto |\tilde{E}(\omega)|^2$.

The lowest angular frequency in this spectrum is matched when q is set to 0. Then we get a peak for

$$-\omega T_{\text{rep}} + \Delta\Phi_{\text{CE}} = 0 \tag{2.19}$$

$$\Rightarrow \quad \omega_0 = \frac{\Delta\Phi_{\text{CE}}}{T_{\text{rep}}} \tag{2.20}$$

$$\Rightarrow \quad f_{\text{CEO}} = \frac{\Delta\Phi_{\text{CE}}}{2\pi T_{\text{rep}}} \ . \tag{2.21}$$

This is the so called carrier-envelope offset frequency.
The next frequency can be obtained by setting $q = 1$:

$$-\omega T_{\text{rep}} + \Delta\Phi_{\text{CE}} + 2\pi = 0 \tag{2.22}$$

$$\Rightarrow \quad \omega_1 = \frac{\Delta\Phi_{\text{CE}} + 2\pi}{T_{\text{rep}}} \tag{2.23}$$

$$\Rightarrow \quad \omega_{\text{rep}} = \omega_1 - \omega_0 = \frac{2\pi}{T_{\text{rep}}} \tag{2.24}$$

$$\Rightarrow \quad f_{\text{rep}} = \frac{1}{T_{\text{rep}}} \ . \tag{2.25}$$

These results can be summarized in the well-known definition of the FC spectrum under an envelope governed by the gain spectrum:

$$f_q = f_{CEO} + q f_{\text{rep}}. \tag{2.26}$$

The repetition time T_{rep} is usually in the lower ns regime [24], [25], so both these frequencies lie in the radio-frequency (RF) domain and can thus be measured electronically.

2.1.3 High Harmonic Generation

There are multiple ways of multiplying the photon energy. One such way is the usage of non-linear optical media leading to second harmonics, another may be four-

wave or sum-frequency generation. Due to a lack of coherent laser-light sources with a sufficiently small bandwidth and considerable total average power output in the XUV-regime, we rely on such non-linear effects in order to do FC-spectroscopy at high frequencies. However, these processes rely on optical media (usually crystals) that do not allow XUV-light to pass through. This brings up the necessity for another process that can be employed here: high harmonic generation (HHG). In short, a gas with a relatively high ionization energy is brought into a region of very high laser intensity giving rise to photon energy multiplication.

In this section, an overview over the the process of HHG is given, following the semi-classical Three-Step-Model (TSM) from Corkum [26].

Step 1

In the first step, the bound electron experiences a force by the electric field of a laser resulting in an additional slope modifying the atomic potential. If the laser intensity is high enough, the bending of the atomic potential is strong enough such that a considerable tunnel probability arises.
In order to describe this ionization process, especially for laser frequencies ω below the ionization threshold ($\hbar\omega < U_{ion}$), it is helpful to define the Keldysh parameter at this point [27]:

$$\gamma = \frac{\omega}{\omega_t} = \omega \frac{\sqrt{2m_e U_{\text{ion}}}}{eE} \ . \tag{2.27}$$

Here, $\omega_t = eI/\sqrt{2m_e U_{\text{ion}}}$ is an estimate for the turn off point from which on the tunnel probability depends on the frequency of the incoming radiation. E is the electric field strength of the laser, m_e the electron mass and e the elementary charge.
This parameter can be used to distinguish the different regimes of the photo-ionization process: If $\gamma \gg 1$, the ionization energy of the electron is much bigger than the energy gained by the laser-field within one optical cycle and thus, multiphoton ionization is the dominant process. For the case of relatively low laser intensities, where the Stark shift is not yet significant, the ionization probability scales with I^N, where N is the number of photons required for this process [28]. In this region, higher laser intensities vastly increase the production efficiency of photons with higher frequencies.

Another key parameter regarding that process is the ponderomotive energy which describes the time averaged energy of a charged particle in an oscillating electric field. For such a particle, the force acting on it can be written as

$$F = qE\cos(\omega t), \tag{2.28}$$

with q being the charge of that particle.
The position of that particle over time is given by

$$x(t) = -\frac{F}{m\omega^2} = -\frac{qE}{m\omega^2}\cos(\omega t). \tag{2.29}$$

Neglecting potential energies yields the ponderomotive energy as the time average of the kinetic part:

$$U_{\text{pond}} = \frac{1}{2}m\omega^2\langle x^2\rangle = \frac{q^2E^2}{4m\omega^2}\ . \tag{2.30}$$

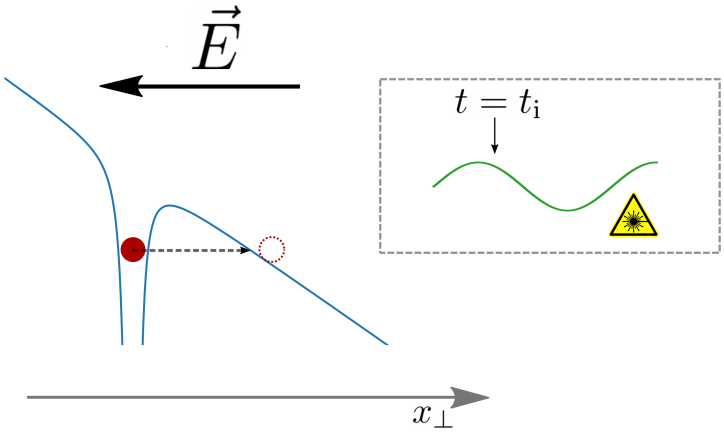

Figure 2.3: In the first step, the atom potential is tilted due to a strong electric field in the vicinity of the atom allowing for tunnelling to happen. The green wave in the box indicates the laser phase of the step, ionization takes place shortly after the electric field reaches the maximum.

With that, we can rewrite the Keldysh parameter as

$$\gamma = \sqrt{\frac{U_{\text{ion}}}{2U_{\text{pond}}}}\ . \tag{2.31}$$

As the ponderomotive potential approaches the ionization potential ($\gamma \sim 1$), the probability of tunnelling out of the atom potential increases such that ionization can happen. Usually, this regime is used in experiments revolving around HHG.

Step 2

As the field gets weaker, the electron still accelerates away from the parent ion and is thus less and less affected by the Coulomb potential making it possible to describe the movement of the electron in a classical way. In this region, the effects of the ion as well as the path modification stemming from the magnetic field are both neglected. For that, we introduce the ionization time $t_\mathrm{i} > 0$ marking the moment in which the electron leaves the area of influence and starts to behave like a free particle. With the boundary condition $v(t_\mathrm{i}) = 0$, we can write down the velocity v for $t > t_\mathrm{i}$ ($E = -E_0 \cos(\omega t)$):

$$v(t) = \frac{eE_0}{m_e\omega}\Big(\sin(\omega t) - \sin(\omega t_\mathrm{i})\Big). \tag{2.32}$$

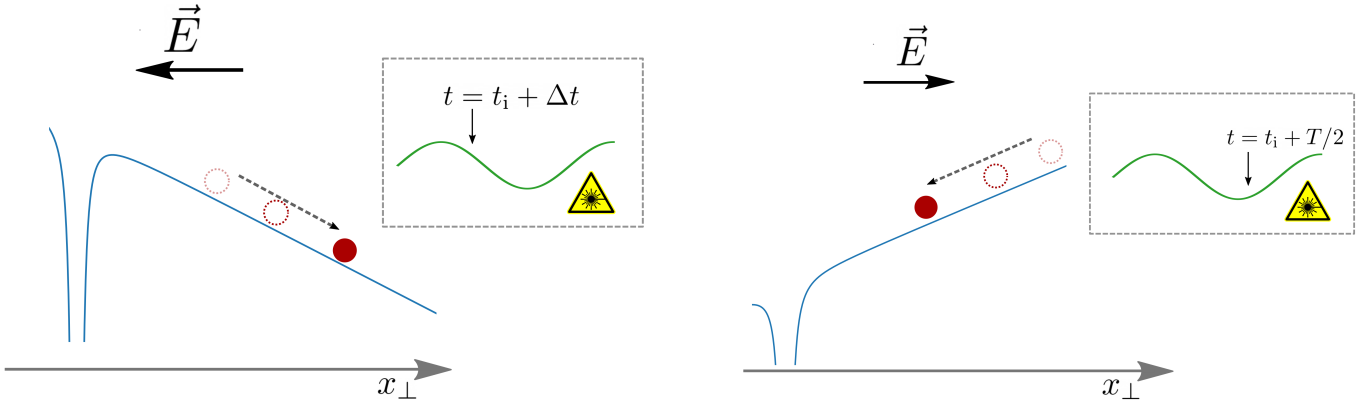

Figure 2.4: If the electron is far away from its parent ion, it can be described as a free particle moving according to classical mechanics. By rolling down the potential landscape, it gains kinetic energy.

Integrating again and substituting t with $\phi = \omega t$ yields the position. The second boundary condition is set by defining the ion position as the origin of the coordinate system ($x(t_\mathrm{i}) = 0$).

$$x(\phi) = \frac{eE_0}{m_e\omega^2}\Big(\cos(\phi_\mathrm{i}) - \cos(\phi) - (\phi - \phi_\mathrm{i})\sin(\phi_\mathrm{i})\Big) \tag{2.33}$$

$$v(\phi) = \frac{eE_0}{m_e\omega}\Big(\sin(\phi) - \sin(\phi_\mathrm{i})\Big). \tag{2.34}$$

As long as the electron does not approach relativistic speeds, we can calculate the kinetic energy by the non-relativist formula $E_\mathrm{kin} = \frac{m_e}{2}v^2$.

Step 3

Still being accelerated in the electric field of the laser, the electron is driven back to its parent ion, able to recombine with it and losing the kinetic energy in the process by emitting a single photon. Since energy can only be deposited in odd multiples of the photon energy hf, the outgoing photon energy must also be a multiple of that ($E_o = n \cdot hf,\ n \in \mathbb{N}$), giving rise to harmonics of the fundamental frequency f.

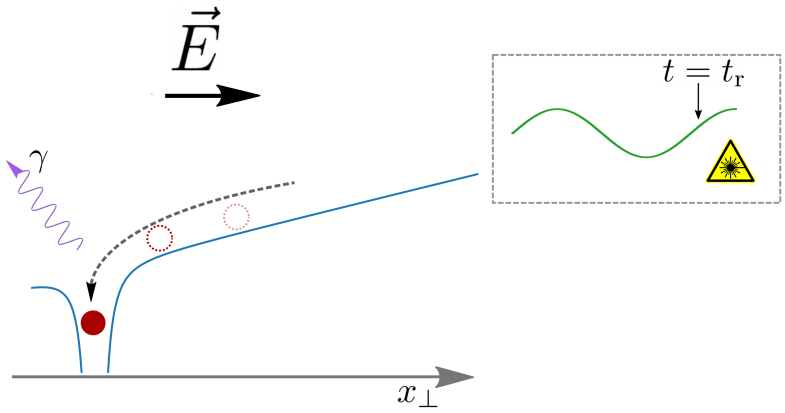

Figure 2.5: The electron recombines with its parent ion and emits a photon of higher frequency with the energy $E_{\text{kin}} + E_{\text{ion}}$ at the recombination time t_r.

Using the Three-Step-Model, we can calculate the maximum energy generated by the HHG process. For that, we take a look at the velocity at the recombination time $v(t_r)$.

As can be seen in Fig. 2.6, various electron trajectories lead to different energies at the point of retrieval. The maximum kinetic energy of the recombining electron can be obtained for a tunnel phase $\phi_i \approx 0.31$, which also marks the most likely value to find [26]. Inserting that number of ϕ_i into Eqn. 2.33 and setting $x(\phi) = 0$ yields the recombination phase $\phi_r \approx 4.4$, which in turn can be used to calculate the kinetic energy of the incoming electron via Eqn. 2.34 resulting in $E_{\text{kin, max}} = 3.17 U_{\text{pond}}$ as the highest possible kinetic energy. Combining that with the ionization potential results in the maximum (or cutoff) energy of the HHG spectrum:

$$E_{\text{cutoff}} = U_{\text{ion}} + 3.17 U_{\text{pond}} \ . \tag{2.35}$$

This is an important result, since it indicates that the highest reachable photon energy not only depends on the incoming intensity and frequency, but also on the generation medium (usually a gas) used for HHG.

As indicated in Fig. 2.6, there are always two trajectories leading to the same

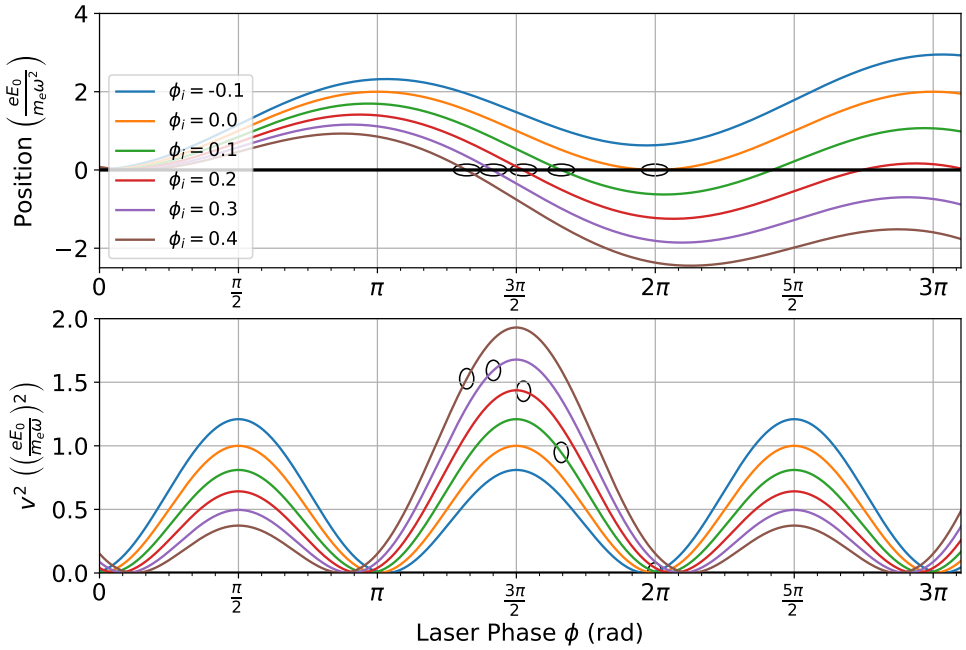

Figure 2.6: Selected trajectories in the 1-dimensional perspective. The black circles show the position and the square of the velocity at the recombination times. Notice how the velocity and with it the final kinetic energy changes with the tunnel phase ϕ_i.

recombination energy. For $\phi_\mathrm{i} < 0.31$, the recombination takes place at $\phi_\mathrm{r} > 4.4$ which describes a long trajectory and for $\phi_\mathrm{i} > 0.31$ we get $\phi_\mathrm{r} < 4.4$ called the short trajectory.

2.2 Beam Propagation

In this section, the behavior of pulse trains in the vacuum especially when focussed to a small spatial volume is briefly discussed, following [29] and [30].

2.2.1 Beam propagation in Ray Optics

Light propagating along the z-direction can be, in the simplest case, described by a plane wave.

$$E(z,t) = E_0 e^{i(\omega t + k_z z)}, \tag{2.36}$$

with the field frequency ω and the wave number in z-direction k_z. If we describe the spatial expansion of the wave perpendicular to the wave-vector as a circle, we can calculate the focussing behaviour of that light entering a thin lens or curved mirrors fairly easily:

$$\frac{1}{f} = \frac{1}{b} + \frac{1}{g} \,, \tag{2.37}$$

with f being the focal length, b the distance from the lens to the image and g the distance to the object set before the lens.
The radius of the beam decreases linearly after passing through the lens and gets infinitely small at the focal point:

$$r(z) = R\left(1 - \frac{z}{f}\right), \tag{2.38}$$

with R denoting the radius of the unfocused beam.

In case, the beam is pointed parallel to the lens axis but with a transversal offset x_0, we still get the same result for the radius across the z dimension, however, the now cone-shaped beam propagates with an angle in respect to the lens axis. This angle is only dependent on the offset and the focal length:

$$\varphi = \arctan(\frac{x_0}{f}). \tag{2.39}$$

2.2.2 Gaussian Beam Propagation

Introducing a non-constant transverse beam profile with a time dependency results in a behavior different to that discussed before. Assuming a propagation in z-direction and a gaussian temporal profile (see Eqn. 2.14), we can write the according electric field with the help of a scalar function $u(x, y, z)$ representing the spatial dependency ($x = y = 0$ represents the beam center):

$$E(x, y, z, t) = \frac{1}{2} u(x, y, z) A(t, z) e^{i(\omega t - k_c z)} + c.c. \,. \tag{2.40}$$

Since the electric field should satisfy Maxwell´s equations, this form can be inserted in Eqn. 2.11. In order to find a solution regarding $u(x, y, z)$, we first assume that the main contribution to changes in z-direction stem from the exponential part. Together with the separation of the time dependent part and a paraxial approximation we get a simplified defining equation for that function:

$$\left(\partial_x^2 + \partial_y^2 - 2ik_c\partial_z\right) u(x,y,z) = 0. \tag{2.41}$$

Under these conditions and approximations, the result resembles a Gauss-shaped transverse profile:

$$u(x,y,z) = \frac{u_0}{\sqrt{1+z^2/\rho_0^2}} e^{-i\Theta(z)} e^{-ik_c(x^2+y^2)/2R(z)} e^{-(x^2+y^2)/w^2(z)}, \tag{2.42}$$

with

$$\text{curvature radius} \qquad R(z) = z + \frac{z_R^2}{z}\ , \tag{2.43}$$

$$\text{beam radius} \qquad w(z) = \frac{FWHM(z)}{\sqrt{2ln2}} = w_0\sqrt{1+\frac{z^2}{z_R^2}}\ , \tag{2.44}$$

$$\text{divergence angle} \qquad \Theta(z) = \arctan(\frac{z}{z_R}), \tag{2.45}$$

$$\text{Rayleigh range} \qquad z_R = \frac{n\pi w_0^2}{\lambda}\ , \tag{2.46}$$

$$\text{asymtote angle} \qquad \theta_0 = \lim_{z\to\infty} \arctan(\frac{w(z)}{z})\ . \tag{2.47}$$

Here, $n = \sqrt{\epsilon_r \mu_r}$ denotes the wavelength dependent refractive index, FWHM stands for the full-width-half-maximum of the spatial distribution. An illustration of the properties of the gaussian beam is given in Fig 2.7. Note that the beam width is one standard deviation of the Gauss-distribution outlining the cross section of the beam and is not to be confused with an edge beyond which the intensity is zero.

2.3 Thermodynamics

In this section, some thermodynamic principles and applications helpful for understanding the process of gas recycling used for the experiment are presented, following [31] and [32].

As a start some very important equations are introduced, governing the behavior of fluids in various circumstances.

Firstly, the ideal gas law should be mentioned, although not universally applicable, especially for high pressures. For reference, according to [33], the compressibility factor defined as $Z = P/\rho RT$ (P: pressure, ρ: molar density, R: universal gas constant, T: absolute temperature), which can be considered as a deviation from

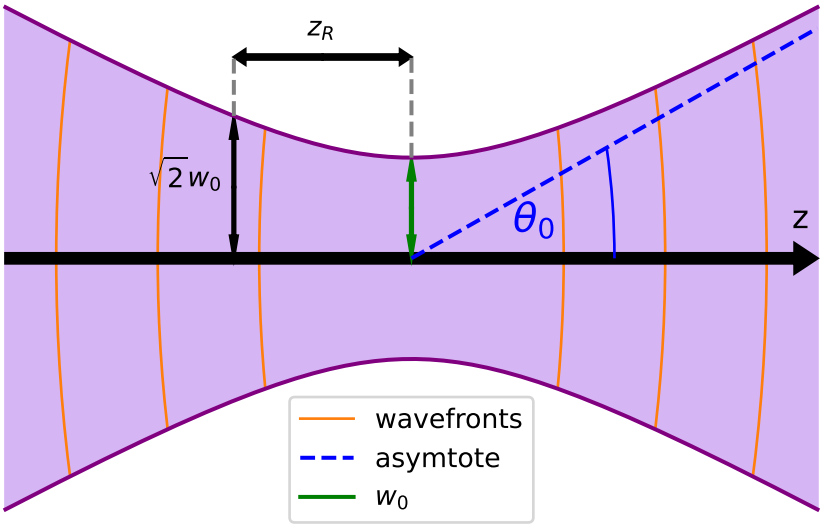

Figure 2.7: Illustration of the Gaussian beam. In contrast to the ray-optics view, the Gaussian beam cannot be focused to an indefinitely small point, but always stays above a certain minimal size w_0. The Rayleigh range z_R is the distance from the focus point at which the beam radius is $\sqrt{2}w_0$.

the ideal gas law, was measured to be $Z = 1.13833$ at a pressure of 286.68 bar and temperature of 323.15 K for nitrogen (N_2). This means that for nitrogen, the actual pressure would be roughly 14 % bigger than the value calculated with the ideal gas law and the corresponding parameters at 286.68 bar. At 100 bar, the deviation is only about 1.7 %.
However, it proves to be well suited for considerations where a high precision is not enormously important. It states that the pressure p, the volume V, the number of particles involved N and the absolute temperature T obey the following relation:

$$pV = Nk_BT \ , \tag{2.48}$$

with the Boltzmann constant $k_B = 1.380\,649 \times 10^{-23}\,\mathrm{J \cdot K^{-1}}$. An important special case directly arising from this equation concerns about a situation where the temperature is fixed. Then we get

$$\frac{pV}{N} = const\ . \tag{2.49}$$

Another important equation describing the mass conservation of a fluid is the continuity equation:

$$\frac{\partial \rho}{\partial t} + \nabla \vec{j} = 0, \tag{2.50}$$

with ρ being the mass density and $\vec{j}$ the mass current density.

Introducing the concept of conservation of energy to hydrodynamics yields the Bernoulli equation, describing flow of a fluid on the basis of energy conservation:

$$\frac{\vec{v}^2}{2} + \frac{p}{\rho} + gz = const. \tag{2.51}$$

Here, $\vec{v}$ is the velocity-vector, g the local gravitational constant and z the relative elevation.
If the change in potential energy is small over a given process, the relation can further be simplified to

$$\frac{v^2}{2} + \frac{p}{\rho} = const. \tag{2.52}$$

3 Experiment

In this chapter, an overview of the experimental setup is given, introducing the most important components and their functions. Although the main chamber of the experiment houses an additional experimental setup regarding velocity map imaging (VMI) [34], we want to focus on the HHG producing part, of which a more detailed description is given in [23] and [35].

3.1 Laser System

Consisting of multiple parts for power amplification, pulse compression and more, the laser system marks the basis of the experiment presented.

3.1.1 Frequency Comb

The starting point of the laser light used for HHG is the oscillator of a phase stabilized NIR frequency comb (Menlo Systems FC1000-250) with a center wavelength of 1039 nm with a FWHM spectral bandwidth of 14 nm, a 100 MHz repetition rate, a pulse length of 24 ps and a maximum averaged output power of 12 W. In order to make use of the FC in spectroscopy, the repetition rate can be changed within a range of $\pm 1\%$. Additionally, the offset frequency f_{CEO} can be altered by influencing the dispersion inside the oscillator.
The repetition rate is stabilized to a fractional uncertainty of 10^{-12} within 1 second by means of a direct digital synthesizer and a phase-locked oscillator.

3.1.2 Amplification and Compression

Upon leaving the laser oscillator with an average power of 10 W and a pulse duration of 24 ps, the laser is amplified and compressed to an average power of around 80 W and a much shorter pulse duration of 200 fs. For further details, see Fig. 3.1.

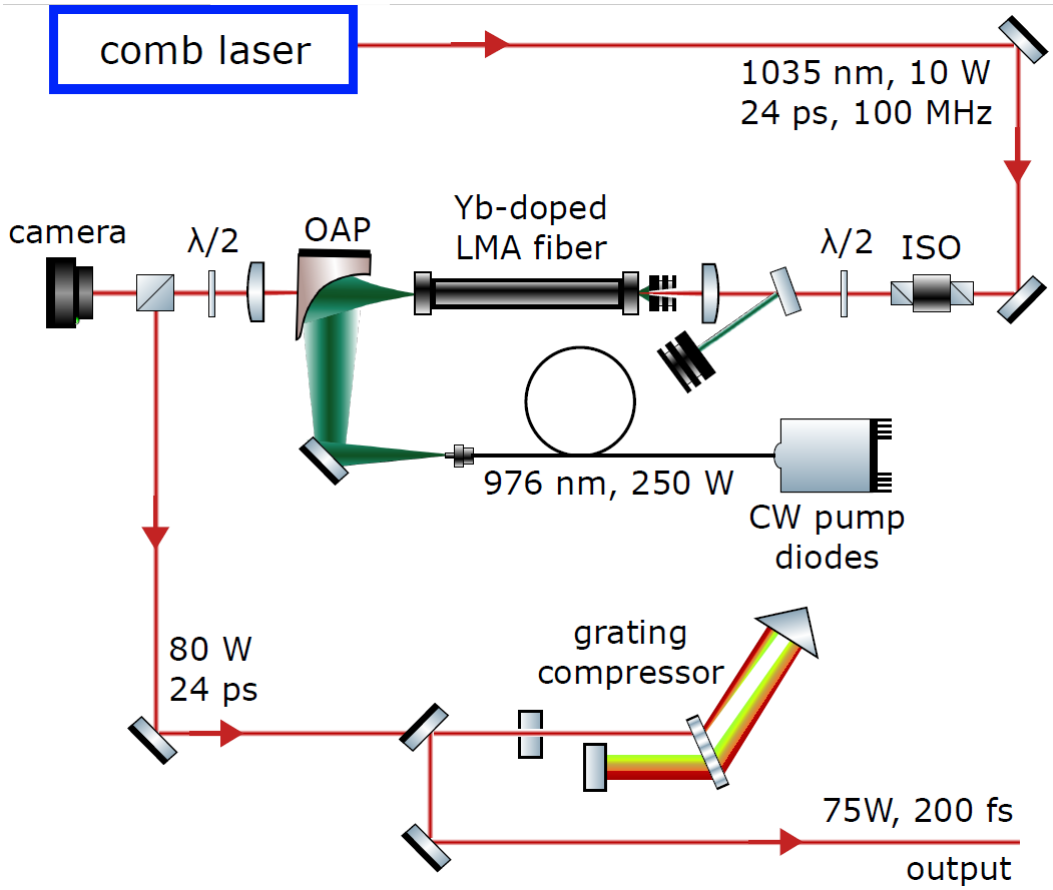

Figure 3.1: Schematic overview over the integral parts of the system before entering the enhancement cavity. An optical isolator (ISO) protects the laser oscillator and the preamplifiers from back-reflections. The beam is then amplified by a 80 cm long Yb-doped photonic crystal fiber rod (aeroGAIN-ROD-MODULE-2.0 PM85, NKT photonics) pumped by a 976 nm, 250 W pump diode (D4F2S22-976.3-250C-IS58.1, DILAS Diodenlaser GmbH) focused by an off-axis parabolic gold-coated mirror with a $\phi = 3$ mm hole on the laser-axis. Passing through the fiber-amplifier increases the average power of the pulse train to roughly 80 W. Afterwards, the pulse train is directed to a grating compressor with a total transmission efficiency of 95%, effectively shortening the pulse duration to 22 fs. Then the compressed laser light enters the enhancement cavity inside the main vacuum chamber. Taken from [23].

3.2 Enhancement Cavity

More details of the XUV comb setup can be found in the dissertation of J. Nauta [23] and a recent publication [35].
HHG requires very high laser intensities in the range of $10^{14}\,\mathrm{W\,cm^{-2}}$ calling for a more sophisticated setting than just focusing the laser onto a gas target. If we assume an average power of 80 W, a repetition rate of 100 MHz and a pulse length

of 220 fs, a beam focused on a circular area with $\phi = 10\,\mu m$ would only reach an intensity in the order of $10^{12}\,W\,cm^{-2}$.
A passive enhancement cavity is an ideal tool to amplify the peak intensities without the need for excessive laser powers, which are not realizable yet. Since the laser beam should be tightly focused to an area as small as possible, the curved mirrors inside such a cavity need to be rather close to the focal point, hence, a bow-tie configuration is chosen (see Fig. 3.2). When choosing the form of the curved mirrors, it must be taken into account that both beam planes (sagittal and tangential) do not necessarily share the same focus, resulting in astigmatism which would decrease the peak intensity. For compensation of this behaviour, two spherically shaped cavity mirrors and one cylindrical input coupler are installed [35].
Since high intensities inside the cavity can only be reached if the pulses overlap, the effective cavity length (path length of one round-trip) must be held constant matching the repetition rate of the laser with high accuracy, which poses a problem: changes in temperature as well as outer disturbances influence the length over time.
Two main conditions have to be met in order to reach the intensities needed. For one, the phase-difference between two superimposing pulses inside the cavity should be a multiple of 2π for constructive interference to happen and secondly, the pulse envelopes must overlap. Consequently, the cavity length must be stabilized to the length of 3 m with a variation significantly smaller than one wavelength (1039 nm), meaning a maximum tolerance of some tens of nanometers must be respected. A linear translation stage combined with a piezo chip has proven as an ideal tool for this task. Placed at the long arm of the cavity, the stage can correct the total length by about 13 mm. To compensate for the minor and rapid vibrations and laser irregularities, a piezo chip is placed on top of the stage realizing continuous changes in length down to a precision of single nm.

It should be noted here, that in principle, additional mirrors can be introduced to match the 3 m path length without increasing the total cavity size. However, introducing more mirror brings in three distinct disadvantages. Firstly, each mirror is a point of energy loss and additional dispersion. Secondly, a system with more mirrors is more susceptible to disturbances. And thirdly, it is unavoidable that any mirror exhibits a certain wear-down over time under such high power conditions, even when used in ultra high vacuum and with an ozone-oxidizing-system. A bigger amount of mirrors makes keeping them clean, aligning them inside the chamber and maintaining them more work intensive.

Making monitoring and diagnostics possible is mandatory for keeping such an enhancement cavity operational given the aforementioned task to stabilize the cavity length. If we cannot gain information about the peak focal intensity inside the cavity focus, there is no way of changing the position of the piezo-controlled mirror effectively. Luckily, there is an easy way of "looking" inside the cavity

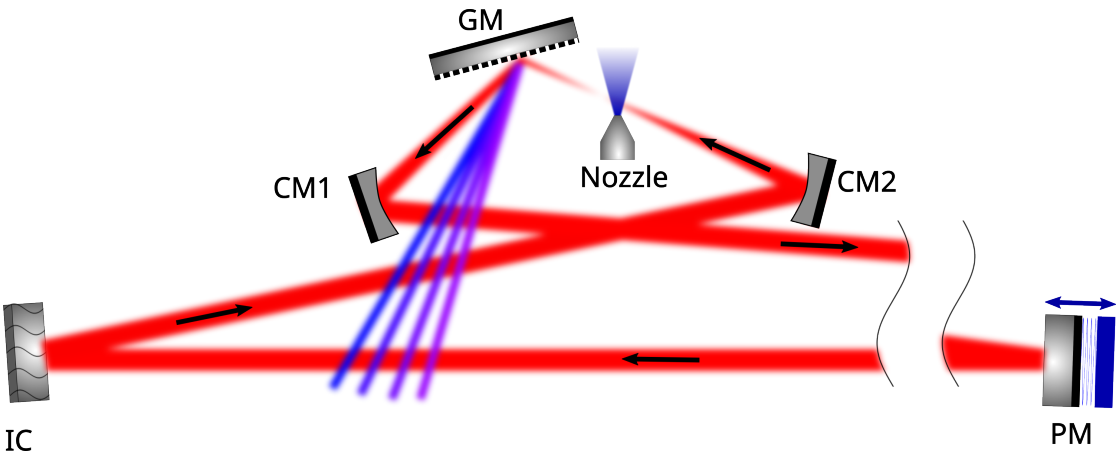

Figure 3.2: Schematic arrangement of the main parts inside the enhancement cavity. The pulses travel in a round trip through the bow-tie formation and overlap with the next one entering the input coupler (IC). The focus defined by the curved mirrors (CM1 and CM2) is set exactly above the nozzle. The mirror mounted on the piezo stage (PM) ensures the effective cavity length stays constant. Upon hitting the grating mirror (GM), the XUV light is decoupled from the laser pulses.

without disturbing the processes inside.

Intensity Measurement

Although mirrors should ideally reflect all of the incoming light, some leakage can never be completely prevented. A useful property of the leakage rate, i.e. the power passing through a mirror, is that it is proportional to the incident power. A photodiode is placed behind CM1 to measure the average power inside the cavity $P_{\mathrm{in}} = P_{\mathrm{PD}}/T$ with P_{in}, P_{PD} being the power inside and on the photodiode, respectively and T being the transmittance. Via the repetition rate and the pulse duration, the peak power of a single pulse can then be calculated and finally, the peak intensity can be determined with the focus area.

Locking

Locking the cavity length is enormously important when high cavity powers should be realized. Here, the Pound-Drever-Hall technique is applied, as modelled in Fig. 3.3. a 4 MHz electro-optical modulator (EOM) instantiates two sidebands onto each tooth of the FC with a spectral distance of 4 MHz from the respective tooth. Since the IC must have a certain transmittance, light cannot only enter the cavity through it, but can also leave once a round-trip is completed. However, constructive interference and thus cavity enhancement only happens if the teeth of the FC are resonant with the cavity. This light can then be focused onto a

fast photodiode and mixed with the original modulator signal to produce an error signal that can be fed to a proportional-integral-derivative (PID) controller that moves the piezo stage and piezo chip ensuring the cavity stays at the resonance length for every frequency of the FC.

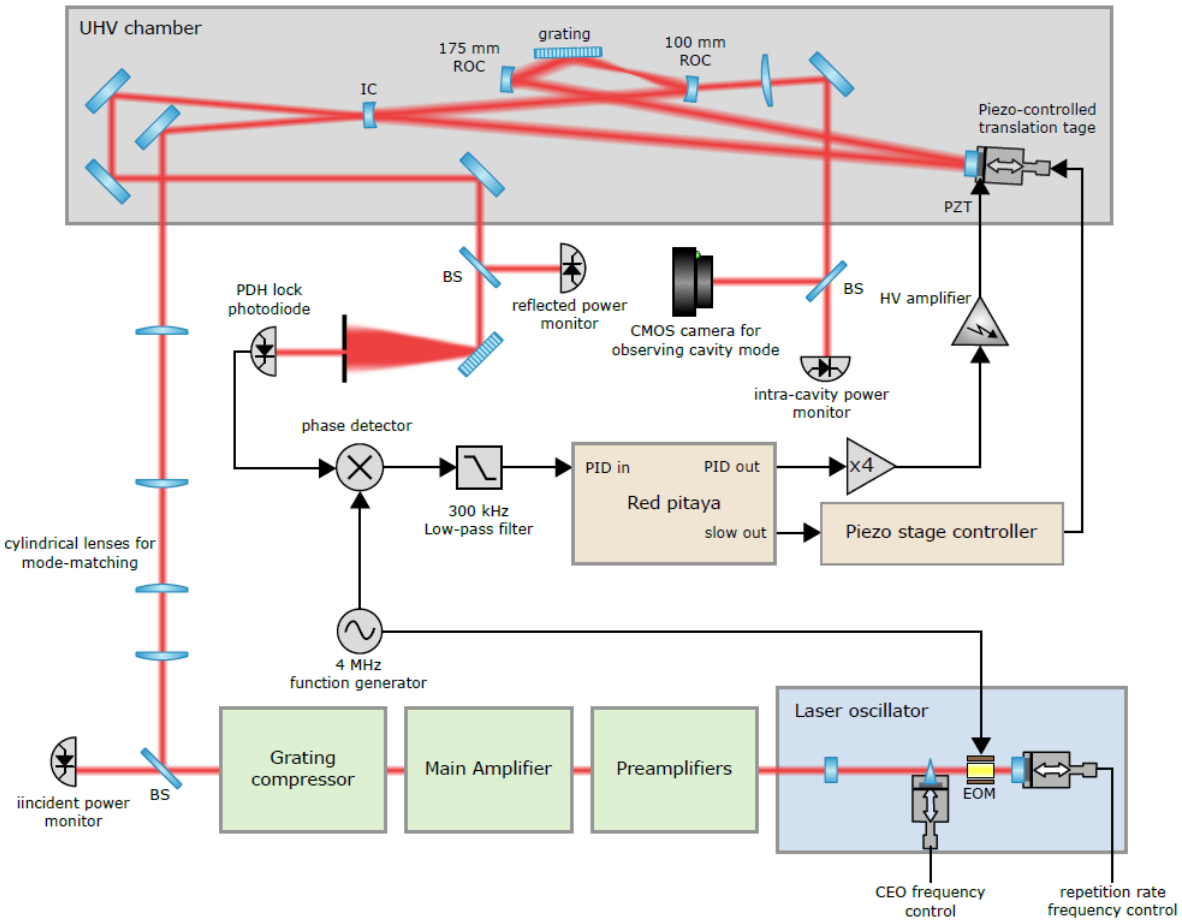

Figure 3.3: Overview of the locking electronics using the Pound-Dever-Hall technique. A radio-frequency is modulated on the laser oscillator, which is reflected by the cavity if all frequency teeth are resonant. The signal is mixed with the direct modulator output and the resulting error signal is fed to a PID-controller ensuring the cavity stays at resonance length. Taken from [34].

3.3 Vacuum System

One of the most important conditions for HHG in the XUV-regime is maintaining a vacuum. The most important reason for that is the opacity of air for UV light rendering low power spectroscopy impossible under a normal atmosphere. Addi-

tionally, the effect of dispersion broadening the ultrashort laser pulses propagating in a medium and therefore reducing the peak intensity must be mentioned. Aside from that, due to the extreme intensities reached in the cavity focus, air in close proximity would be ionized, decreasing the power usable for HHG.
There is another reason aside from that, why an UHV regime should be employed here: a long term goal of the entire experiment is to do XUV spectroscopy with single HCI trapped inside a cryogenic Paul-trap (CryPTEx) [36, 37]. Since this trap needs to operate at a pressure of about 10^{-14} mbar, and the beamline connecting the trap and the cavity has to be continuous, a problem arises when injecting a gas jet with a backing pressure of 10 bar into the cavity focus.
Maintaining such a pressure gradient inside the chamber over time makes a differential pumping system necessary. For the specific implementations, see [38, 23, 39].

Such a differential pumping system consists of multiple vacuum pumps (in our case turbo-molecular pumps (TMPs)) placed spatially apart from each other. The most important part of the system employed in the setup of this experiment is placed directly above the gas jet nozzle consisting of three turbo pumps acting on skimmers layered around each other making a stationary pressure gradient inside the vacuum chamber possible.

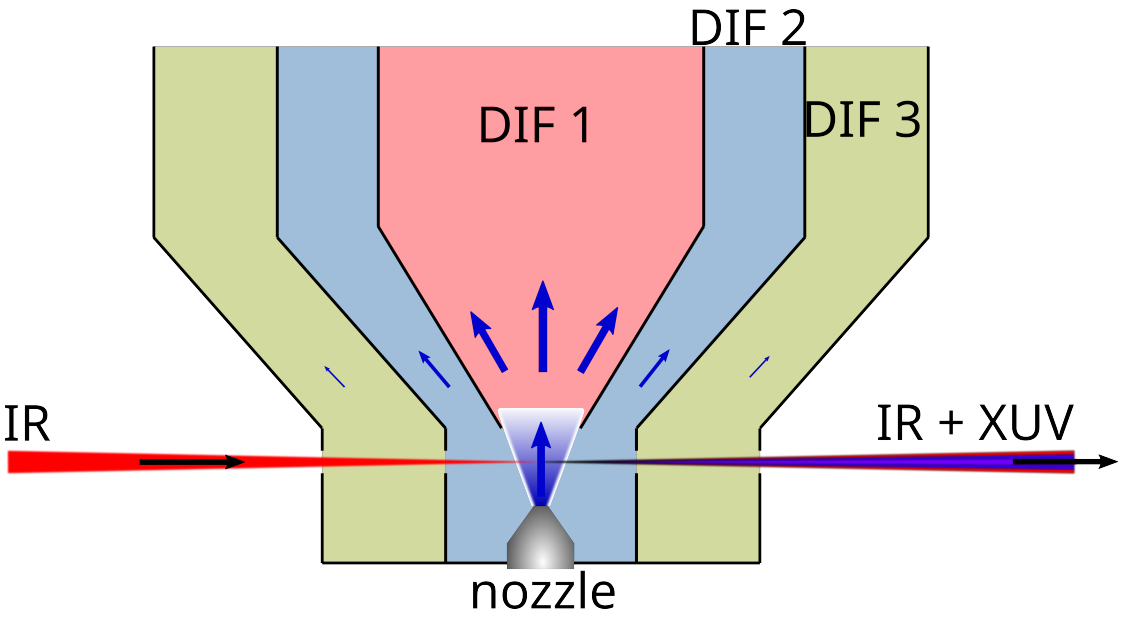

Figure 3.4: Illustration of the conically shaped compartments of the differential pumping system shown in Fig. 3.6. IR-light enters the focus and HHG takes place. Three different pumping stages (DIF1, DIF2, DIF3) are placed directly above the nozzle, collecting the gas used for HHG (not to scale).

This system ensures a sufficient vacuum in the range of about 10^{-7} mbar inside

the main chamber while allowing a high pressure gas jet inside the focal region.

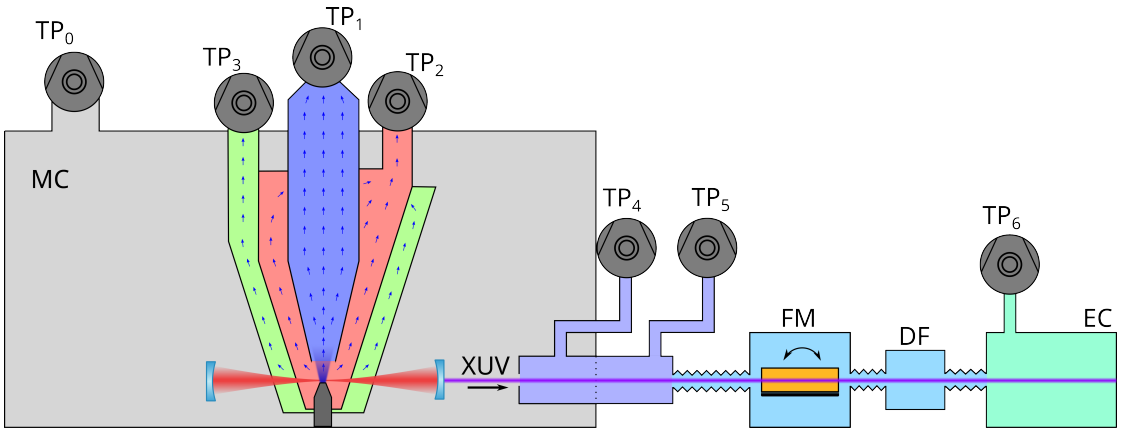

Figure 3.5: Pumping system of the cavity and beamline. The outcoupled XUV light leaves the main chamber (MC) through flexible bellows, hits the toroidal focusing mirror (FM) and transverses through the diagnostics flange (DF) into the experimental chamber (EC). The three TMPs $TP_{4,5,6}$ installed along the beamline build up the pressure gradient.

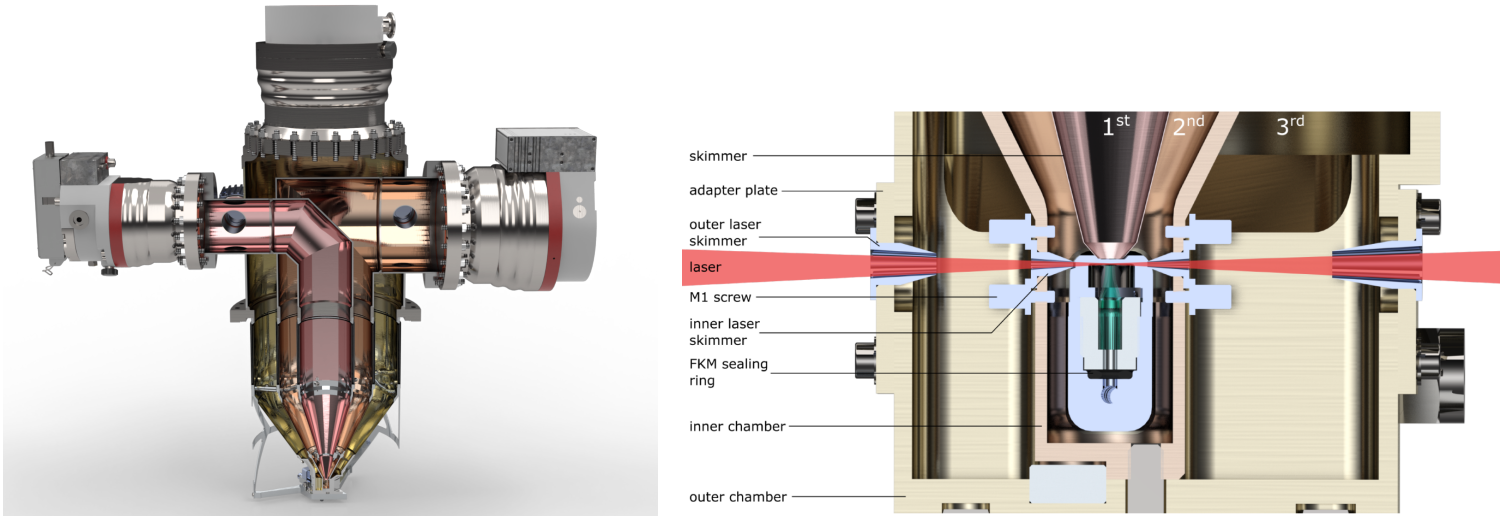

(a) Overview **(b)** Nozzle region

Figure 3.6: 3D models of the differential pump system directly above the nozzle. The thin inner laser skimmers make sure that only very little gas enters the main chamber. Each compartment is evacuated with a separate TMP. Taken from [23].

Decoupling the pressure of the experimental chamber, which will later be replaced by the Paul-trap of the CryPTEx II experiment, from the cavity, allows for pressures reaching further down than 10^{-7} mbar. Fig. 3.5 shows the specific arrangement of the turbo pumps used for this. The main pump (TP_0) and the three

pumps of the differential pump system ($TP_{1,2,3}$) ensure a sufficient vacuum inside the main chamber. A flexible bellow attached to the short end of the main chamber marks the outset of the beamline. Three additional TMPs ($TP_{4,5,6}$) guarantee a sufficient pressure gradient towards the experimental chamber.

Since the TMPs are not designed to establish high pressure differences, but rather to extract remnants of gas particles, their backing pressure should ideally be significantly below atmospheric pressure. For this purpose, scroll pumps are applied, functioning as fore-vacuum pumps. To use the differential pumping system for the recycling of target gas, some valves were installed to select which turbo pump feeds which fore-vacuum pump. For more details see Fig. 3.4.

3.3.1 Ozone System

Because contamination with various substances inside the cavity is unavoidable, even under UHV conditions, mirror deterioration is to be reckoned with. Especially hydrocarbons can contribute to mirror contamination because of the high photon energies of the XUV light - and to some extent the high NIR laser intensities - splitting up the bigger molecules leaving behind carbon compounds staining the mirrors over time. For this reason, nozzles have been installed in front of the mirrors introducing ozone (O_3) to protect the surfaces. The goal of this is to oxidize any remnant carbon compound before it can settle on the mirrors.

Principally, the pressure inside the main chamber can be kept at around 10^{-8} mbar for extended periods of time. However, this ozone combined with the introduced target gas for HHG causes the minimally achievable pressure to rise to roughly 10^{-4} mbar.

3.4 Beamline

Merely producing XUV light in the cavity is not enough for XUV spectroscopy. For one, light inside the cavity travels in roundtrips, making an outcoupling device (in our case a grating mirror) necessary. Secondly, the outcoupled XUV light needs to be focussed to a small region to maximize the intensity in the vicinity of the target. Additionally, the pressure at the target location has to be substantially smaller ($\approx 10^{-14}$ mbar) than in the main chamber. All of these factors require the construction of a separate beamline. The considerations in planning of that beamline as well as its implementations are further explained in [40].

Because the harmonic orders all have different wavelengths, their angles of diffraction also differ. For gratings, the following equation describing the relation between incident angle θ_{in} and outgoing angle θ_{out} holds:

$$\sin(\theta_{\text{out}}) = \sin(\theta_{\text{in}}) - \frac{\text{m}\lambda}{d} \ , \tag{3.1}$$

where m denotes the diffraction order, λ the wavelength of the incoming light and d the distance between the ridges of the grating.
Since the higher diffraction orders have less intensity, we can concentrate on the case m$= -1$ here. Additionally, the different harmonic orders also have different wavelengths resulting in different diffraction angles. Accessing all of those harmonic orders within the first diffraction order later makes spectroscopy in a wider frequency range possible. For this, a gold mirror is used to direct light out of the main chamber towards the focussing mirror.

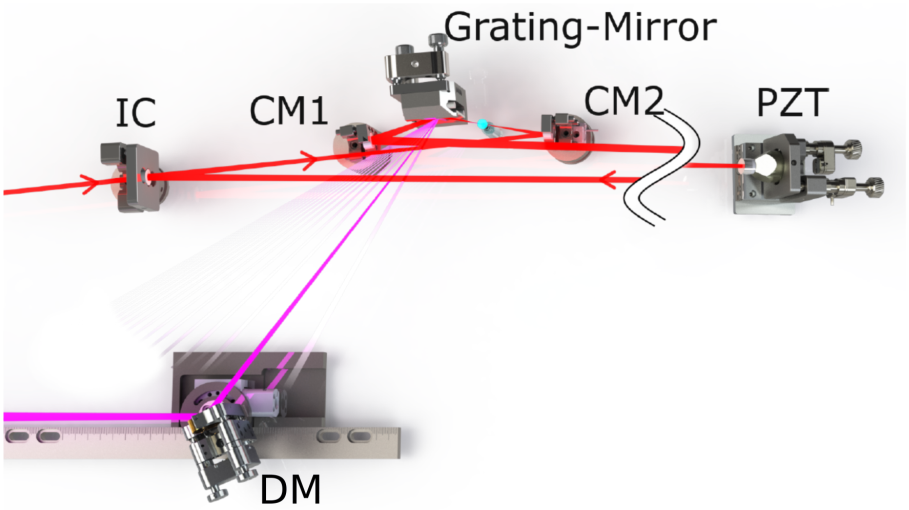

Figure 3.7: Positioning of the directing mirror (DM) used to redirect one outcoupled harmonic order to the beamline. The mount can be rotated as well as shifted transversally. Adapted from [40].

Next, the beam hits a toroidal gold mirror placed inside a cubic compartment connected to the main chamber by a flexible bellow. Attached to a translation stage, the position of this focussing mirror can be modified along the two horizontal axes. After that, the light enters the diagnostics flange and the experimental chamber (for further explanation, see Section 3.6).

3.5 Gas Recycling system

One of the key challenges of producing high harmonics inside the enhancement cavity is the need for a continuous supply of the gas used in the nozzle. Principally,

every mono-atomic gas could be used for this purpose. However, due to practical reasons such as oxidizing behavior, or the need for high pressures, we stick to the non radioactive noble gases helium, neon, argon, krypton and xenon, especially the latter three. As discussed before, the lighter ones of these can be used to reach higher harmonic orders due to their higher ionization potentials (see Eqn. 2.35). The trade-off for this is a lower overall yield with the same input intensity, which is the reason why often times xenon is used. Xenon on the other hand carries large costs with it when compared to the other noble gases, easily getting to 15 €/SL at the time of writing this thesis (one standard liter, SL, is the amount of gas 1 liter has at norm conditions, i.e. 273.15 K, 1000 mbar). For this reason, a system for gas recycling is of great utility if the cavity is under continuous operation for an extended period of time.

This recycling system consist of three main compartments: a low pressure side (LPS), a compressor station (CS) and a high pressure side (HPS).
For simplicity, all pressure specifications are given in absolute values, i.e. 0 bar meaning vacuum.

Low Pressure Side

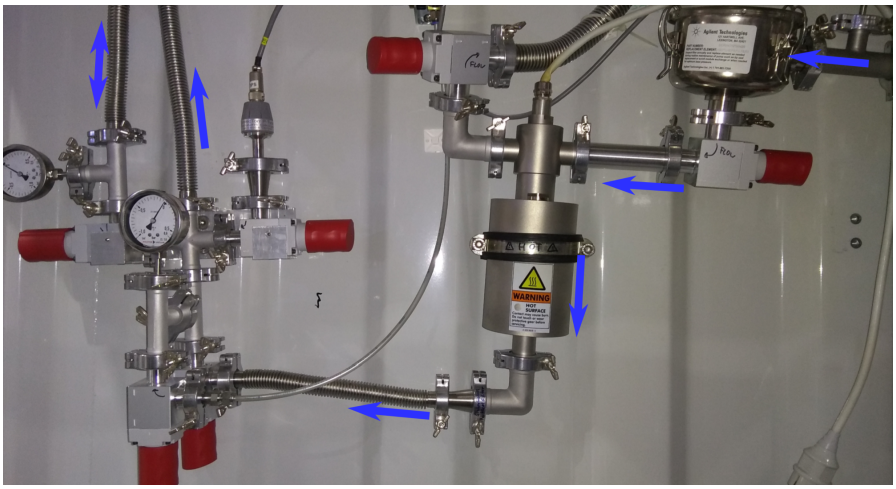

Figure 3.8: Setup of the LPS. Gas enters either via the exhaust of the SP set behind the turbo pumps through the filters, or comes directly from an external gas bottle. It is then stored in a 20 L tank and directed to the CS. The flow direction of target gas during recycling is indicated by the blue arrows.

After entering the differential pumping system, the collected gas is directed to one of the fore-vacuum pumps depending on the setting of the valves (for detailed description see Fig. 3.11). In the next step, the gas is either directed to an external exhaust port (and therefore lost), or confined in the LPS, which is mainly built of a 20 L tank able to store gas of a pressure between 0 and 1 bar, connector

bellows and digital as well as analogue pressure gauges. Before entering the LPS, the gas passes through a particle filter (Agilent Technologies, SCRINTRPNW25) and a water filter (Vacom, FT25KF-J; Adsorption Trap). The total volume of this compartment amounts to 22.2 L, which ends in the input side of the CS. The 20 L tank can be decoupled from the system by closing a valve. In order to fill the system with a utility gas, a gas bottle can be connected to it with a pressure regulator in between.

Compressor Station

Figure 3.9: Structure of the Compressor Station.

For HHG a target gas pressure between 5 bar and 50 bar is required, making a compression mandatory. Setting the pressure on the HPS to a higher value also has the additional benefit of being able to store the same amount of gas in a much smaller volume. For this purpose, a CS (HD-tech) using the compressor types AAD-5 and AA-30 are installed right after a membrane pump to convert the gas to atmospheric pressure. The first compressor brings the pressure of the gas up to around 7 bar stored in a 2 L intermediate tank (IT), leading to the second compressor converting the pressure up to 200 bar. Both of these compressors use an oil free graphite sealing in order to avoid contamination of the target gas. This has two main disadvantages. Firstly, the space between the piston and the cylinder wall might not bee entirely air sealed, letting gas permeate. Secondly, the compressors must be operated at frequencies as low as possible ($\lesssim$ 1 Hz) to avoid premature wear due to friction.
Both of these compressors use the continuous compressed air supply (CAS) of the

facility. The output pressure of these compressors is manually regulated with two pressure reducers between the CAS and the compressors.

Two pressure gauges will be installed at the CS, one between the membrane pump and the first compressor, and one between the compressors, being necessary for the calculation of the total amount of gas in the recycling system.

High Pressure Side

Upon entering the HPS, the compressed gas is cleaned by two filters (Parker Balston Model 95S6, volume: 0.03 L; Parker Balston Model EU37/12, volume: 0.17 L), sorting out remaining water and particles introduced by the CS and pumps. Subsequently, it is stored in a 75 cm^3 tank, decoupling the nozzle flow rate from the compression cycles. In total, the HPS has a volume of 0.29 L, accounting for roughly the same amount of gas as the LPS at a working pressure of 100 bar. With the exception of some smaller pieces and valves, all of the pipes used in the HPS have an inner diameter of 2 mm, making up only about 5.3% of its total volume at a length of 4.9 m. A pressure regulator marking the HPS output reduces the pressure to a set value entering the nozzle, which closes the cycle. Recording the pressure of the HPS will be done with a pressure gauge (IPS-M12 175-4995) set behind the filters employable for pressures up to 250 bar.

Because filling the entire recycling system with the target gas requires the investment of large amount of gas, a valve panel inside the container allows the direct usage of gas to be injected in the nozzle from a gas bottle. Additionally, the gas can also be directed to the velocity-map imaging (VMI) experiment inside the main chamber. A pressure gauge attached to the panel can be used to monitor the backing pressure of the nozzle.

Table 3.1: Summary of the volumes distributed across the different parts.

Position	Volume
LPS	22.2 L
IT	2.041 L
HPS	0.290 L
Nozzle part	0.021 L

3.5.1 Measurement

In order to characterize the efficiency of the recycling system, various pressure gauges have been installed. Because the pressure of the gas in use changes by multiple orders of magnitude throughout one cycle, four different types of gauges are used:

Figure 3.10: Control panel of the HPS. Gas enters from the CS at a pressure of 10 to 200 bar, passes two filters and is stored in a $75\,\mathrm{cm}^3$ tank. The pressure outlet leading to the nozzle is controlled manually via a pressure reducer.

1.) vacuum gauge (0 to 1000 mbar), Leybold IONIVAC ITR 90, digital output

2.) 1.33×10^{-4} to 1000 mbar tube sensor, Agilent Varian ConvecTorr p-type

3.) 0 to 25 bar, IPS-M12 Pressure Sensor, type: 175-4981, 4 to 20 mA output

4.) 1 to 26 bar, IPS-M12 Pressure Sensor, type: 175-4992, 4 to 20 mA output

5.) 1 to 251 bar, IPS-M12 Pressure Sensor, type: 175-4995, 4 to 20 mA output

While the first two types output a digital signal and can be read out directly, the latter three give an output current between 4 and 20 mA according to the signal. They use a temperature-compensated piezo-resistive ceramic sensor. In contrast to this, the vacuum gauges use a hot-cathode ionization sensor combined with a Pirani-type sensor.

For the simultaneous readout of the pressure values of these two analogue gauges, a converter box has been built. This box consists of four input plugs for the four-pin connector cables, four independent voltage sources providing the gauges with the necessary voltage of 12 V and a 4-channel, 4 to 20 mA ADC converter shield connected to an Arduino-Nano board.

In order to ensure the voltage supply of the pressure gauges that need to be in the range of 9 to 32 V, the 5 V output of the Arduino board feeds four independent voltage converters boosting the voltage up to 12 V. The independent converters protect the system against potential ground-loops distorting the measured signals. One pin per outlet is set to 12 V, the second one goes over one of the current readout channels of the ADC and further to the system ground. Since the pressure gauges

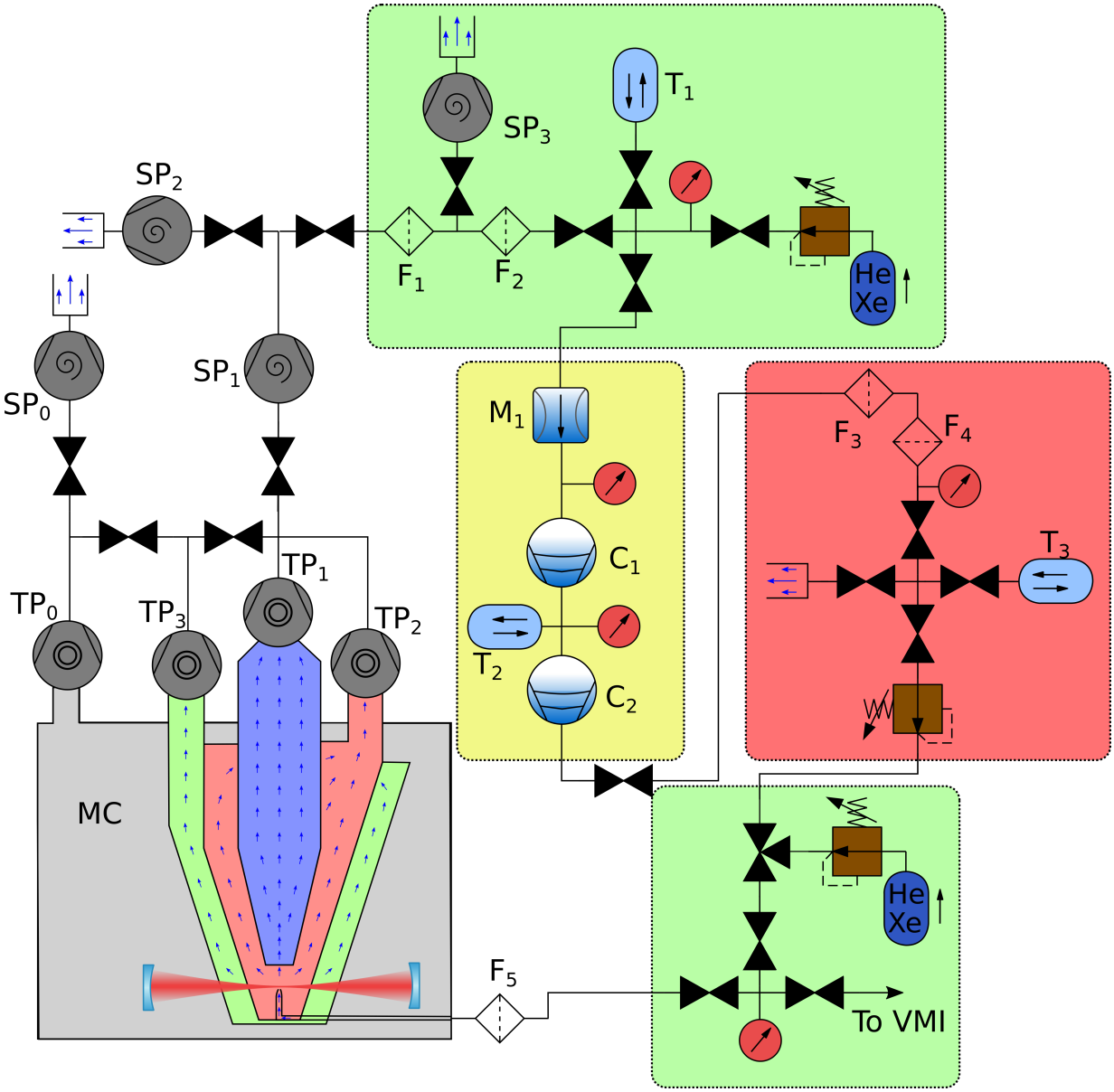

Figure 3.11: Integral parts of the Gas-Recycling system. The valves directly behind the turbo-pumps can be used to select the parts of the vacuum system that should be recycled. The storage capacities of the tanks are T_1: $20\,l$, T_2: $2\,l$, T_3: $0.075\,l$. Only the digital pressure gauges are shown here.
Legend: TP $\hat{=}$ turbo-pumps, SP $\hat{=}$ scroll-pumps, F $\hat{=}$ filter, T $\hat{=}$ tanks, C $\hat{=}$ compressors, MC $\hat{=}$ main chamber.

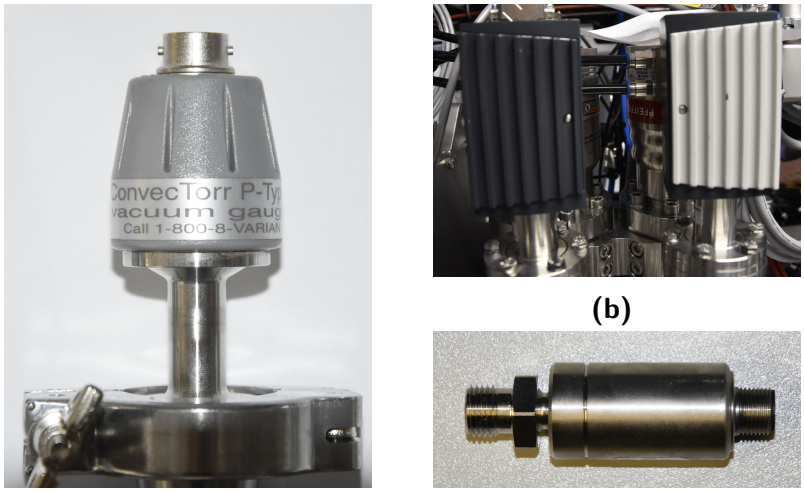

(a) **(b)** **(c)**

Figure 3.12: In the vacuum, and gas system, different types of pressure sensors are used, depending on the pressure ranges.
(a) 0 to 1 bar gauge for fore-vacuum pumps and LPS
(b) Vacuum gauge for precision measurement
(c) IPS-M12 pressure-sensor for high pressures

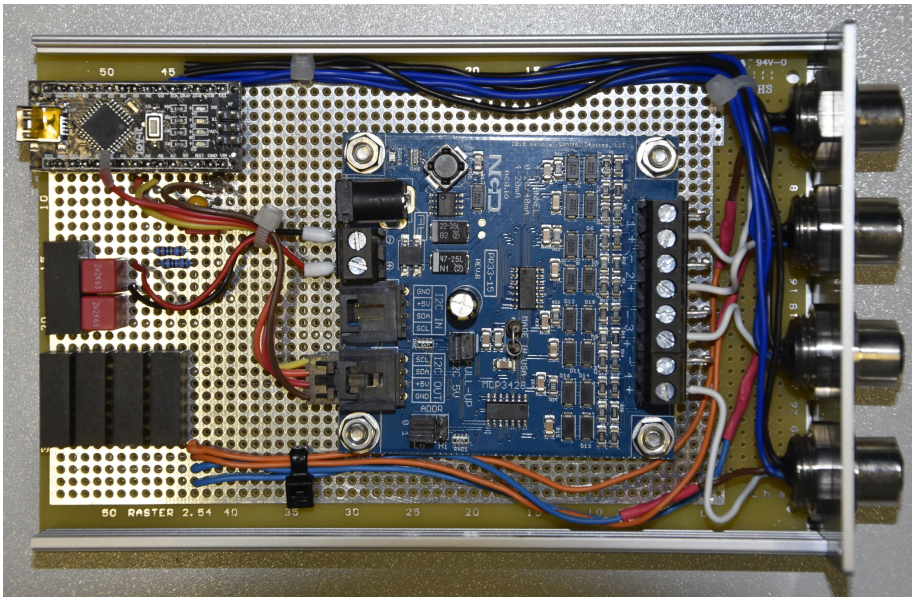

Figure 3.13: Setup of the measuring device used for readout of the high-pressure values. The power supply as well as the data communication is provided by the micro-USB plug of the Arduino-board.

will allow a current to flow between 4 and 20 mA, with a linear dependence of the pressure applied, the system can easily detect any malfunction regarding the

gauges if a current of less than 4 mA is measured.

3.6 Laser Alignment System

Due to the fact that HHG is a process that is highly sensitive to the effective intensity in the conversion region, the laser used for it must be stable throughout the process. This proves to be quite difficult, because thermal expansion and mechanical disturbances influence the laser resonator as well as the cavity and might disturb cavity locking. Additional disturbances during HHG, like mechanical vibrations, must be kept to a minimum, making further adjustments during HHG difficult. Moreover, even if mechanical disturbances could be compensated, identifying the path of the XUV beam is not an easy task, since the XUV power is in the order of µW and can only be detected using fluorescent screens, making long exposure times necessary. For these reasons, the optical elements are best adjusted before the cavity length is locked.

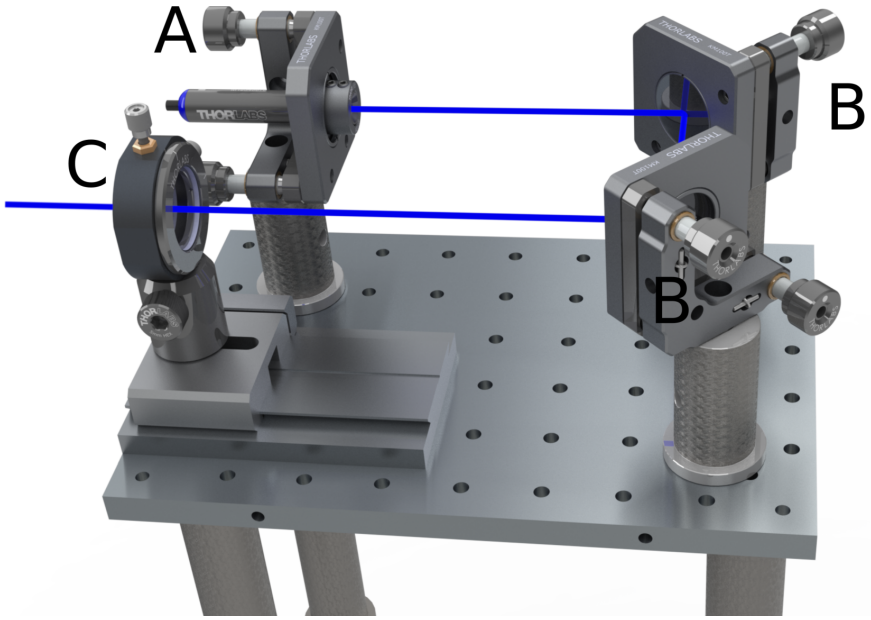

Figure 3.14: Alignment table with laser. The laser (A) is placed roughly anti-parallel to the beamline, two adjustable mirrors (B) are used to fine-adjust the light on the beamline axis. A lens (C) on an axial translation stage with a 300 mm focal length focusses the laser beam to the same spot as the XUV light guided by the toroidal mirror.

One way to achieve this is to employ an alignment laser in the visible spectrum to use as a proxy for the XUV-light. For practical reasons, a positioning of such an additional laser source inside the cavity is not advisable, however, a backwards propagating beam serves the same purpose, and is easier to implement.

The idea behind the laser alignment system is to put the mirrors for steering the XUV light in the right place before powering up the enhancement cavity. If the light from the alignment laser goes through the focus of the experimental chamber and hits the grating mirror inside the cavity on the same spot as the XUV light, the latter will propagate along the same path in the opposite direction.
Adding two mirrors allows for smaller corrections in height of the beam without needing to adjust the laser holder directly, and therefore makes finding the correct height easier.

Ensuring that the laser beam travels through the focus of the experimental chamber is done via a 300 mm focal length lens, a razor blade and a CCD camera as seen in Fig. 3.15.

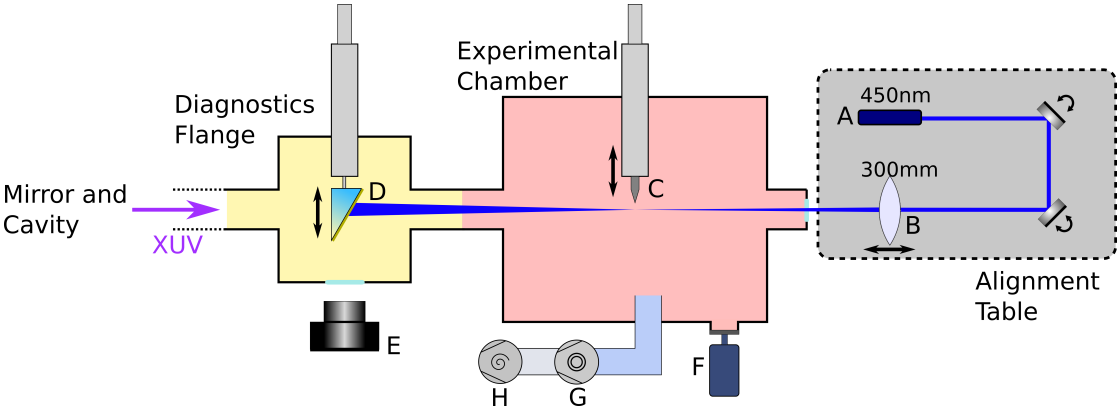

Figure 3.15: Setup for focal point calibration. The laser source (A) is focused by a lens (B) into the focal point where a razor blade (C) is driven into. The remaining light hits a screen coated with sodium salicylate (D) inside the diagnostics flange and is monitored by a CCD camera (E). Monitoring the pressure inside the experimental chamber is done via a vacuum pressure gauge (F). A turbo pump (G), combined with a scroll pump (H) ensures UHV conditions. If the coated screen and the photodiode are retracted, the light hits the gold mirror and then enters the cavity, pointing at the grating mirror where the scattered light can be detected.

The razor blade and the fluorescent glass plate with the photodiode can be moved by means of linear vacuum feedthroughs. That way, the focal size of the alignment laser can be measured and the entire beamline can be cleared for XUV light to pass without opening the chambers by retracting the feedthrough holders. Coating the glass plate with sodium salicylate has the advantage that visible light gets scattered and XUV light is made visible because of the fluorescent property of that material. This is the reason, why we use a 450 nm laser, because the scattered wavelength is in the same range as the fluorescent light of the sodium salacylate.
Additionally, the diagnostics flange has been equipped with another linear feedthrough holding a retractable photodiode to measure the total power of the incident XUV light.

4 Characterization of the Gas-Recycling System

In this part, we want to examine the working principle, efficiency and functional boundaries of the gas-recycling system developed by J.-H. Oelmann with the purpose of reducing the loss of valuable noble gases such as xenon used for HHG.

4.1 Leakproofness of the System

One important parameter for the description of the recycling system is the amount of gas that is lost over time through leaks. Gas can be lost in many different ways throughout the whole compression cycle.
Firstly, one of the larger contributing factors is the presence of small leaks mainly in the connecting pieces. If the parts (mostly consisting of metals) do not have tight contact at all points, some gas will inevitably leave the system. This is especially true, if the pressure inside the system is high in comparison to the environment, which means that the HPS is especially vulnerable to this kind of leakage. Luckily, larger leaks in overpressure systems (those which have a higher pressure than the environment) are relatively easy to find with a leak detector if the type of gas inside is known and not very abundant in the atmosphere. For this reason, often times helium is used, since its relative abundance in the lower atmosphere of the earth is only around 5.5 ppm [41]. Two of the most notable points of loss are the spaces between the pistons and the cylinder walls inside the compressors. To avoid contamination with oily substances, they use graphite sealing, which does not entirely prohibit gas flow.
Another rather uncontrollable way in which gas gets lost in the cycle is via diffusion through sealing materials and the metal walls. Since all materials show this behavior to some degree, it cannot be entirely compensated. This is especially a problem with smaller molecules and atoms, such as helium.
Thirdly, we have to consider that not all the pumps ensuring a vacuum inside the main chamber are used to feed the gas back in the cycle (see Fig. 3.11). The main reason for that is to prevent contamination of the target gas with ozone used to slow down mirror degradation. Too much ozone could damage the compressors and might alter the properties of the HHG process.

For these reasons, probing the system for overall losses in different situations is useful for estimating its effectiveness. Moreover, knowledge over relative proportions

of these factors makes improving the whole system easier.

4.1.1 The Loss over Time

In a first trial, before the above-atmosphere pressure gauges were available, the leakproofness of the system parts outside the container has been examined. This was done by closing the valve after the scroll pump on the LPS and the pressure regulator after the HPS. Since the compressors should not come into contact with larger amounts of oxygen to prevent degradation, the system was then filled with argon, which is cheaper than xenon, but as a noble gas still nonreactive. With the pressure of the LPS held at a constant value of around 1 bar, the driving pressures of the two compressors are gradually increased in order to bring the HPS pressure to 52 bar. Afterwards, the argon bottle inlet is closed, such that the system is operated in a closed loop. Now, as long as there is still some gas left on the LPS, the pressure on the HPS is kept roughly constant, which was confirmed regularly by checking an analogue pressure gauge every 24 hours. The compressors themselves will always keep the outlet pressure to a value that is solely dependent on the CAS pressure used to compress the gas. The outlet pressure will ideally stay at a constant value according to

$$p_{\text{out}} = r p_{\text{w}} \ , \tag{4.1}$$

where r is the pre-set transmission ratio ($r_1 = 5$ for the first compressor and $r_2 = 30$ for the second) and p_{w} the CAS pressure used to compress the target gas.

Because the pressure of the LPS is limited to 1 bar abs. (atmospheric pressure or below), losses of the gas in this specific configuration can only be attributed to the CS or the HPS. Fig. 4.1 shows the experimental results of the according measurement.

As we can see in Fig. 4.1, the pressure decreases in a roughly linear fashion across time. However, the curve is modulated by seemingly periodic oscillations with increasing amplitude. Additionally, some outliers as well as longer irregularities can be seen.

The linear behavior of the pressure curve can be explained by assuming one or multiple small leaks on the HPS or the CS with a loss rate proportional to the pressure difference between the inside and outside of the system. Because the CS always ensures a constant outlet pressure (assuming a constant working pressure p_{w} and enough gas inside the LPS), the overall loss rate would be constant over time and thus a linear behavior is expected because the pressure drops only on the LPS.

Fitting a linear curve to the dataset will yield an overall loss rate as the slope

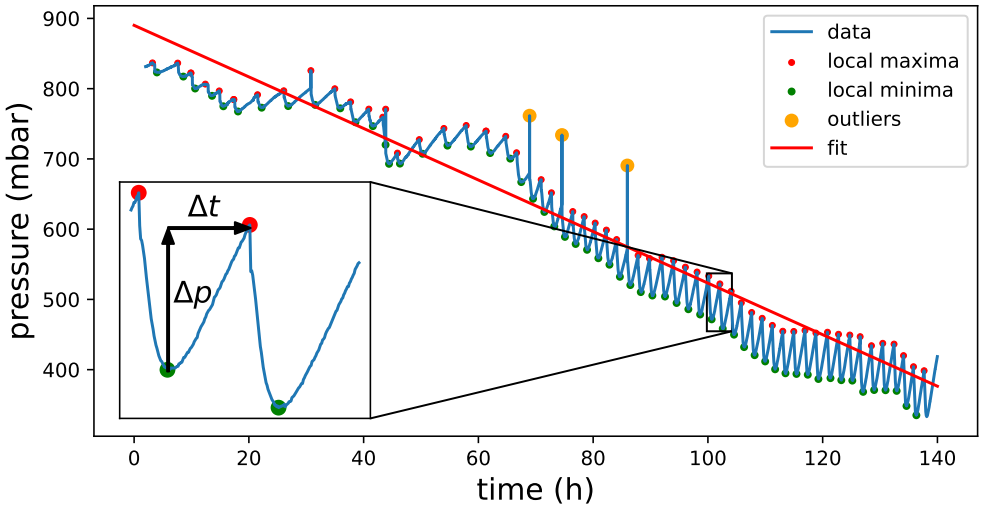

Figure 4.1: Pressure of the LPS during a 7-days measurement with closed valves before the LPS segment and after the HPS. A linear function was fitted to the measured values to show the overall trend.

(dp/dt) is proportional to the lost number of molecules N over time:

$$\frac{dN}{dt} \propto V\frac{dp}{dt} \,, \tag{4.2}$$

where V is the total volume of the LPS, which stays constant.

Since the normal volume is proportional to the number of molecules inside a system, we can calculate this normal volume using the ideal gas law:

$$V_N = V\frac{p}{p_0}\frac{T_0}{T} \tag{4.3}$$

where T is the temperature and $p_0 = 10^5\,\mathrm{Pa}$ and $T_0 = 273.15\,\mathrm{K}$ are the normal pressure and normal temperature respectively.

As the surface area of the LPS is relatively large compared to its volume, since flexible bellows made of stainless steel have been used, the LPS (and arguably also the HPS) is in thermal equilibrium with the air around it.

For the first measurement regarding the leakproofness of the recycling-system, we get a total loss of $(-3.749 \pm 0.007)\,\mathrm{mbar/h}$. According to Eqn. 4.3, a temperature of $T = (20 \pm 3)\,^\circ\mathrm{C}$ and a volume from Table 3.1 this corresponds to a total loss rate of $(0.078 \pm 0.002)\,\mathrm{Sl/h}$. Here, we assumed that the pressure of the HPS stayed constant throughout the measurement, which was confirmed by periodically reading of the analogue pressure gauge.

However, a couple of things have to be considered here. As can be clearly seen in Fig. 4.1, the pressure curve does not strictly follow a linear path. On larger scales (multiple hours), we get broad irregularities like the one between $t = 50\,\mathrm{h}$ and $t = 70\,\mathrm{h}$, which might arise from slow variances of the CAS pressure or temperature fluctuations. Much more important to our investigation are the smaller periodic rising and falling edges which all show a similar form and duration, however they get more pronounced over time. The falling edges are expected, because we assume that the HPS and/or the CS exhibit some leaks. Therefore, gas gets lost over time, but the pressure on the HPS always stays roughly equal as can be seen in Eqn. 4.1. Since the gas has to come from somewhere, the amount stored on the LPS decreases. Because the transport of gas occurs in compression cycles, the pressure decreases in relatively little time. On the other hand, the preceding membrane pump and the response time of the pressure gauge might stretch this steep decrease in the data. What happens right after such a dip should not occur, if the valves behind the pumps used for recycling are closed. If the pressure increased on the LPS and gas can flow towards the HPS, but cannot go back, than that means that some gas has to come from another source. The main part of the pressure rise is probably due to leaks allowing air from the outside to flow into the system if the pressure inside is lower. A control of all the connection pieces might suppress this unwanted behavior, which has to be kept as low as possible, since it is the largest contributor to contamination of the target gas with other substances.
There are further possible contributions for this pressure increase. In addition to the flow of air into the LPS-system, the one-way valve directly in front of the compressor prohibiting compressed gas to flow back into the LPS could be damaged, allowing some gas to flow back. Jumps and fluctuations in the readout signal of the pressure gauges have to be considered too.

Leakage analysis In order to estimate the leakage rate of the LPS, the local maxima and minima have to be identified first and the outliers excluded by hand to get the proper intervals of the rising edges. Such outliers have been observed occasionally without any apparent reason, when the control system of the pressure gauges briefly shows a value that is much higher or lower than directly before and after. These values have to be excluded from our consideration as they do not reflect any physical behavior.

From the intervals, whose edges are defined by one maximum and one minimum, an average slope can be calculated by dividing the pressure difference Δp by the time duration Δt of each interval. Fig. 4.2 shows the positive slopes plotted against the time at which they occur.

Finally, these slopes can be plotted against the pressure difference to the outside world ($p_0 = 1013\,\mathrm{mbar}$) instead of time to get an idea of how the pressure difference influences the leakage rate. The result of this can be seen in Fig. 4.3.

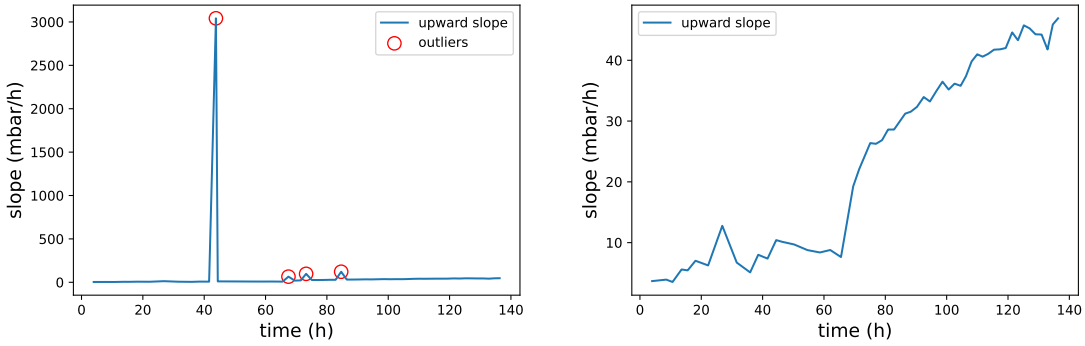

(a) without elimination **(b)** with elimination

Figure 4.2: Course of the upward slope over time. Leaving out some outliers, which can mostly be attributed to electronic errors, results in a rising trend, meaning that the rate at which gas is sucked into the LPS increases over time.

Including all datapoints yields for the slope of the entire plot a value of $(0.0955 \pm 0.0017)\,\mathrm{mbar/h/mbar}$. Using Eqn. 4.3 again, results in the standard volume that is lost over time per mbar of pressure difference:

$$\frac{d}{dp}\frac{dV_{n,\uparrow}}{dt} = (1.942 \pm 0.041) \times 10^{-3}\,\frac{\mathrm{SL/h}}{\mathrm{mbar}}\ ,$$

meaning that if we would pump the LPS empty, around 2 SL of gas would flow in per hour, contaminating the target gas inside. Here, the reduced χ^2-sum is 4.15.

However, there is an unexpected offset:

$$\left.\frac{dp}{dt}\right|_{\Delta p=0} = (-16.8 \pm 0.8)\,\mathrm{mbar/h} \quad \hat{=} \quad (0.341 \pm 0.016)\,\mathrm{SL/h}\ .$$

A possible explanation for this discrepancy might lay a problem with the pressure gauge used here (Agilent Varian ConvecTorr p-type), which is built for a range between 1.33×10^{-4} mbar to 1000 mbar, but shows an increasing uncertainty with higher pressures. A calibration might be useful in the future to avoid these unwanted offsets.

A crude way to get around this problem is to only include datapoints with lower pressure. If we neglect all those with a pressure difference smaller than 350 mbar, not only the residuals get smaller, but the offset is also reduced. Fig. 4.3 shows the data for this case.

The fit-function describing the plot can be stated with the following values:

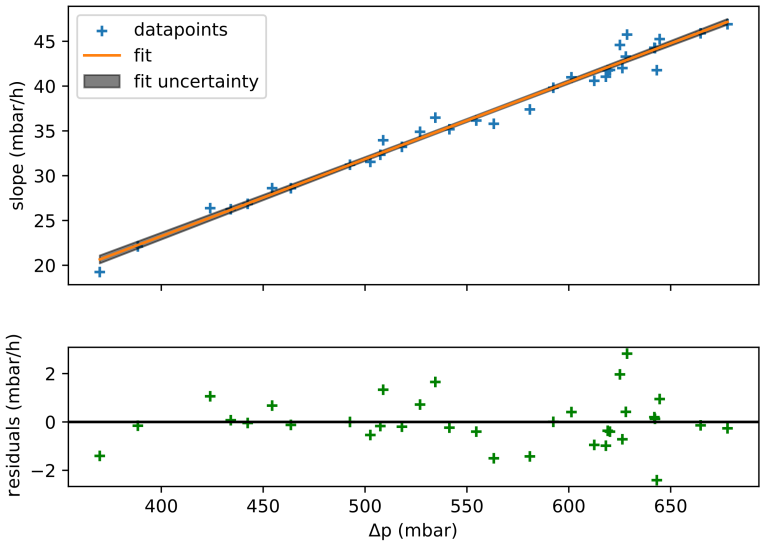

Figure 4.3: Pressure increase of ascending edges against pressure difference to the outside. A linear curve was fitted to the datapoints to show the strict dependence on the pressure difference to the outside. Only datapoints with a pressure difference bigger than $350\,\mathrm{mbar}$ are included.

$$\frac{dp}{dt} = (86.1 \pm 2.1) \times 10^{-3}\,\frac{\mathrm{mbar/h}}{\mathrm{mbar}} \cdot \Delta p - (11.2 \pm 1.2)\,\mathrm{mbar/h}\ ,$$

or equivalently:

$$\frac{dV_{n,\uparrow}}{dt} = (1.751 \pm 0.043)\,\frac{\mathrm{SL/h}}{\mathrm{mbar}} \cdot \Delta p - (0.228 \pm 0.024)\,\mathrm{Sl/h}\ .$$

Directly comparing that value with the one we got above shows a significant difference merely by dismissing the values of pressures too close to the atmospheric pressure.

A reduced χ^2 sum of 1.10 regarding the last fit shows a good correspondence between the data and the assumption that a difference in pressure is proportional to the amount of gas flowing in.

4.1.2 Leakproofness of the Compressor Station

An additional source of loss (or contamination with other gases) is the CS. With its many tubes, two active compressors, a membrane pump, barometers, the interme-

diary tank and some valves, checking it for leaks is important to the functionality of the whole system. In order to do that, a measurement has been carried out, where the entry of the LPS has been blocked as well as the valve on the HPS connecting the CS to the crossing. Unfortunately, the pressure gauge monitoring the HPS was not available at the time of this measurement, however, the pressure value has been controlled multiple times throughout it via a manometer attached to the CS and no significant change has been observed.
Important to notice here is, that some of the leaks of the LPS have been removed in the mean time, making the in-flow weaker.

After evacuating the whole LPS system and emptying the CS and HPS, the CS outlet was closed and the LPS filled with argon gas until the pressure inside stabilized. Subsequently, the argon inlet was closed and the driving pressure set, such that the outlet pressure was set to 100 bar.

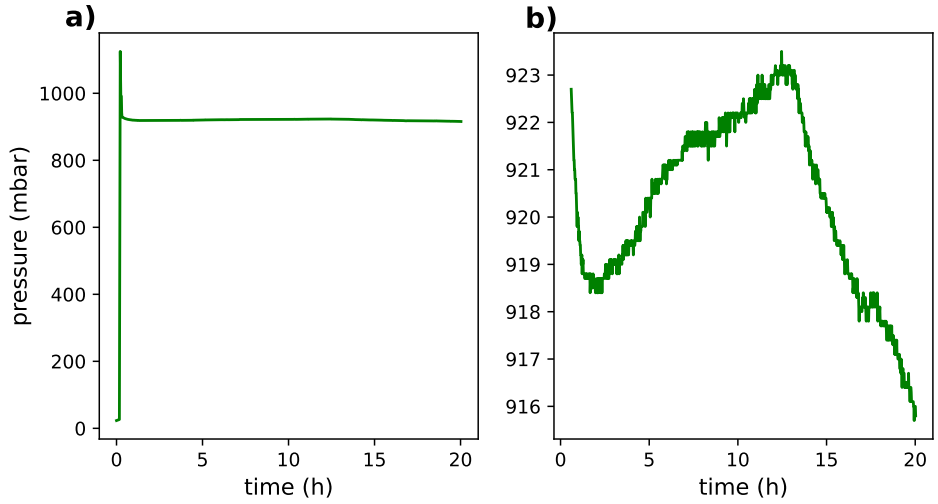

Figure 4.4: Course of the LPS pressure for the measurement regarding the leakproofness of the CS. In a), the overall recorded data is shown, dominated by the large pressure differences while filling, in b), the same data is shown, however, the first few minutes are left out.

In Fig. 4.4, the recorded pressure is shown for this specific setup. As can be seen, at first the pressure rises to a level of more than atmospheric pressure only to fall down to a value of around 920 mbar, where it basically stays until the end of the measurement. The reason for the overshoot might lay in a delayed response of the pressure sensor, since only a single datapoint exhibits a value greater than 1000 mbar. In contrast to Fig. 4.1, no overall loss can be directly attributed to the curve by merely looking at it. If only the datapoints that come after the filling process are taken into account, we can see that the pressure inside the LPS varies only by about 10 mbar, which is equivalent to roughly 0.2 SL, over the course of

20 hours.
Interestingly, between 2 and 12 hours after the measurement started, the pressure inside increased by around 4 mbar. This could be either because of gas still flowing in from the outside, or due to variances in temperature changing the sensitivity of the pressure gauge in use, or changes in atmospheric pressure acting on the membrane bellows and therefore acting on the pressure inside.

In this measurement, we have to include the pressure inside the intermediary tank as well, since it could also exhibit some leaks that might play a role. However, at the time of this measurement, no sensitive pressure gauge that can be read out electronically was installed. Thus, we had to rely on an analogue pressure gauge to check if the pressure stayed constant. Here, a decrease in pressure from 9.2 bar to 9.1 bar within 2 hours was noticed, however, due to a lack of enough datapoints, this rate could not be verified. Further measurements with installed pressure gauges might give more insight here.
The constancy of the LPS pressure after the filling process shows that not a single compression cycle was executed, and therefore, the intermediary tank lost less gas than one such cycle would transmit.

4.2 Nozzle Consumption

Another parameter important for the description of the gas recycling system is the amount of gas that flows through the nozzle. The nozzle has a diameter of 20 µm and can be controlled with some valves inside the container and a pressure regulator used to vary the amount of gas that flows into the chamber. Measuring the amount of gas that is pumped through the nozzle combined with the losses at full recycling allows us to estimate the economic efficiency of the system.

4.2.1 Nozzle Consumption at 8.4 bar backing pressure

For the following measurement, the LPS and the HPS are filled with argon, such that the LPS was at 1050 mbar, the intermediary tank at 6.8 bar and the HPS at 53 bar. The nozzle backing pressure started with 8.4 bar, inside the main chamber 2.6×10^{-5} mbar were measured.

Fig. 4.5 shows the development of the pressure in the different parts of the recycling system for a nozzle backing pressure of roughly 8.4 bar. The latter one stays almost constant over time and even increases towards the end which might be due to uncertainties in measurement or the behavior of the pressure regulator: if the backing pressure falls, the outlet pressure rises to a small extent. Because of this, the HPS pressure should stay constant over time. The other compartments show a steady decline in pressure over time, the most notable being the LPS.

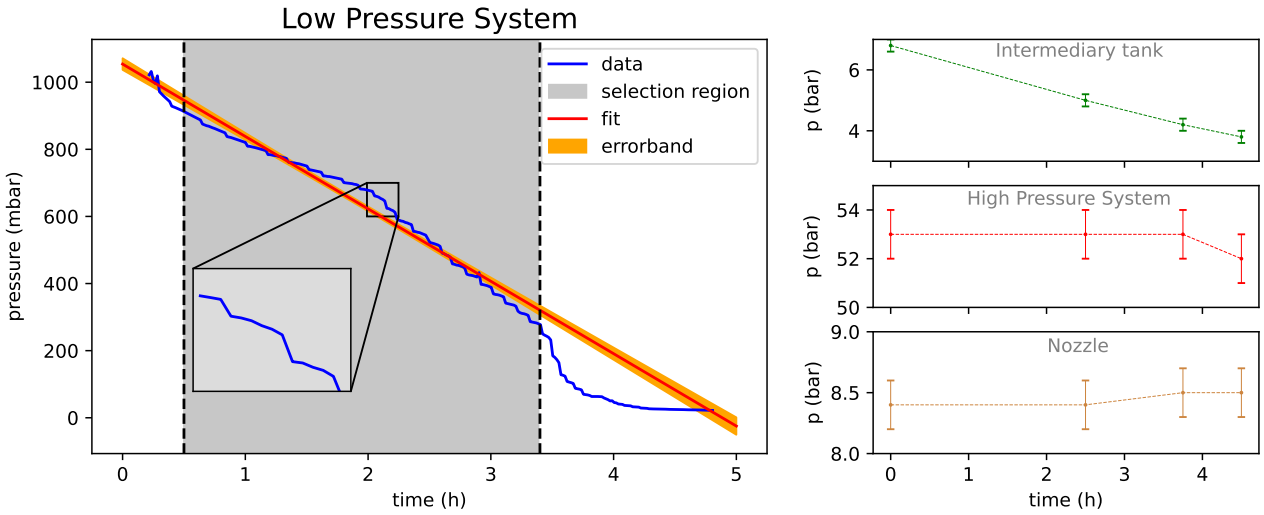

Figure 4.5: Pressures inside the different compartments over time. A decrease in pressure can be seen in all of them except the nozzle backing pressure. The datapoints for the LPS are logged automatically, whereas the other ones are documented by hand. A linear function is fitted to the LPS datapoints using the data between $t = 0.5\,\mathrm{h}$ and $3.4\,\mathrm{h}$.

The reason for the deviation from a linear function regarding the LPS here, is the fact, that the driving pressure of the first compressor had to be changed throughout the measurement for it not to take damage due to a frequency that was too high. This also explains, why the pressure of the intermediary tank does not stay equal over time, contrary to Eqn. 4.1.

In order to estimate the amount of gas, the nozzle consumes over time, the contributions of the different compartments are added up. For the LPS, fitting a linear function to the data has the advantage of outliers at the beginning or end not distorting the value too much, whereas fitting a function to the datasets of the other compartments will not be as effective, since there are not as many datapoints there. For these datasets, the amount of gas lost per time interval can be estimated by dividing the total difference in pressure by the total measurement time.

Table 4.1: Portions of nozzle consumption for different compartments at a backing pressure of $8.4\,\mathrm{bar}$.

Compartment	$\Delta p/\Delta t$	$\Delta V_n/\Delta t$
LPS	$-215.8\,\mathrm{mbar/h}$	$-4.463\,\mathrm{SL/h}$
IT	$-666.6\,\mathrm{mbar/h}$	$-1.268\,\mathrm{SL/h}$
HPS	$-222.2\,\mathrm{mbar/h}$	$-0.060\,\mathrm{SL/h}$
Nozzle part	$22.2\,\mathrm{mbar/h}$	$0.000\,47\,\mathrm{SL/h}$

As can be seen in Tab. 4.1, the loss in the LPS plays a dominant role, even if larger portions of gas leaves the system and the CAS pressure is varied. Again, this is because the pressures in the compartments closer to the nozzle stay roughly constant throughout the process until the LPS is almost empty.
Combining the contributions yields the nozzle consumption at a backing pressure of 8.4 bar:

$$\frac{dV_n}{dt} \approx \sum_i \frac{\Delta V_{n,i}}{\Delta t} = -5.79\,\mathrm{SL/h}\ ,$$

meaning that even with a backing pressure of only 8.4 bar, almost 6 SL of xenon are needed every hour of operation. A gas price of roughly 15 €/SL would result in operation costs between 80 and 90 € per hour.

Ensuring vacuum conditions inside the main chamber is mandatory, especially under cavity operation, which is why a measurement was performed of the pressure regarding the main chamber and the differential pumping system when the nozzle is active.

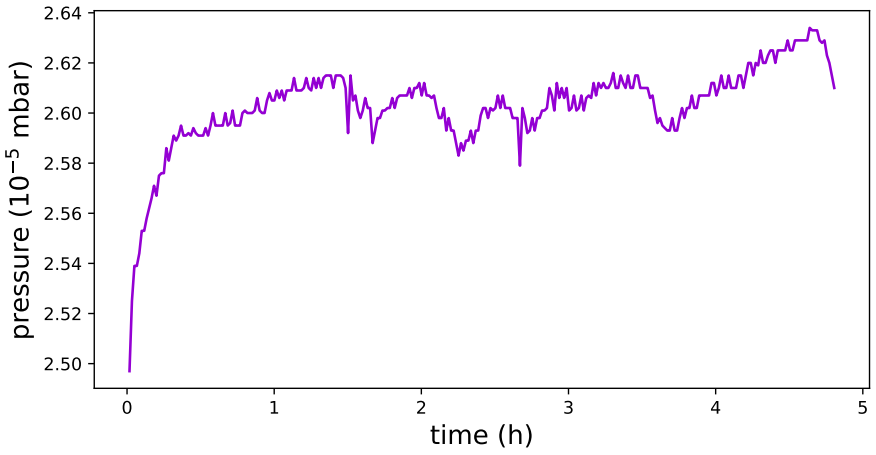

Figure 4.6: Course of the pressure inside the main chamber during measurement of nozzle consumption. The data was recorded with a Leybold IONIVAC ITR 90 vacuum gauge. Not shown is the starting value of 1.428×10^{-7} mbar before gas injection.

As can be seen in Fig. 4.6, the pressure inside the chamber stays at a value of roughly 2.6×10^{-5} mbar when the nozzle is operated at 8.4 mbar. However, there is also a steep increase in pressure once the valve is opened: Within about 20 minutes, the pressure rises from 1.4×10^{-7} mbar to 2.6×10^{-5} mbar. This means that the nozzle strongly influences the pressure inside the cavity, but the differential pumping system is able to hold the pressure always below 10^{-4} mbar.

Fig. 4.7 shows the necessity of a differential pumping system.

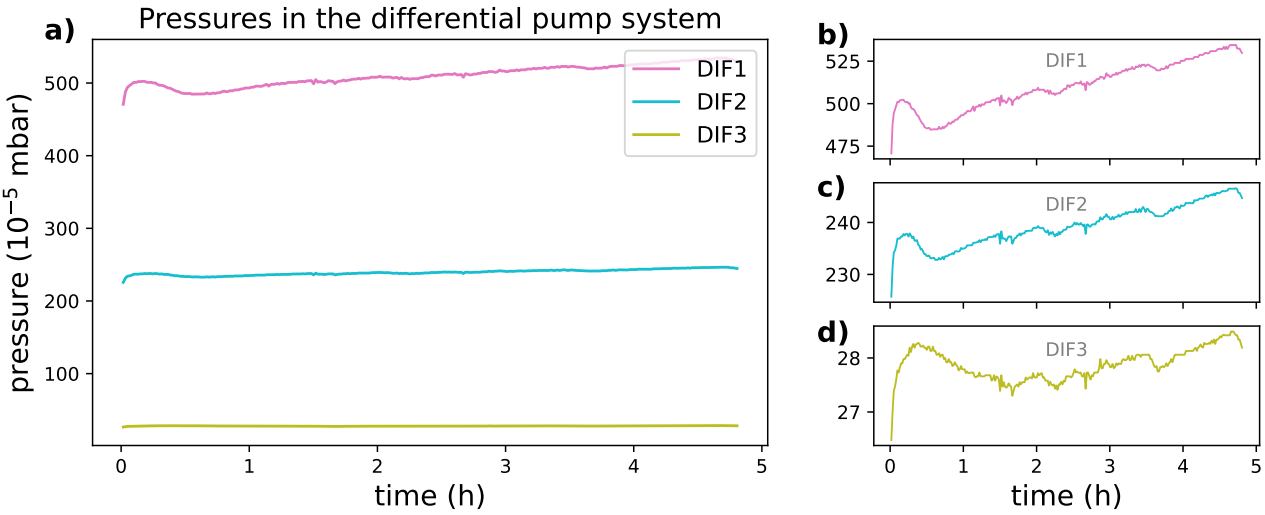

Figure 4.7: Course of the pressures inside the three compartments of the differential pumping system (DIF). Here, DIF1 is placed directly above the nozzle, DIF2 is wrapped around that and in turn contained by the DIF3 compartment. See Fig. 3.4 for reference. Again, the first value is discarded.

In Fig. 4.7, we can see that the differential pumping system makes a steep pressure gradient inside the chamber possible. Equipped with three TMPs, a reduction from 5×10^{-3} mbar to 2.8×10^{-4} mbar can be achieved from DIF1 to DIF3. Qualitatively, all three curves show a similar behavior: at first the pressure rises from about 10^{-8} mbar to a much higher value (in the order of 10^{-3} mbar), overshoots a little, decreases for some time and then increases slowly over the course of the measurement. The overshooting effect at the beginning, lasting up to two hours in the DIF3 compartment, might be due to some gas being injected into the main chamber at the beginning of the measurement.

After reaching a minimum following the subsiding of the overshoot, the pressure rises in a roughly linear fashion indicating again that gas accumulates over time directly below the turbo pumps. The rate of pressure increase is more pronounced in the compartments containing a higher pressure. Since the variations in pressure over the measurement time is in the lower percentage range, statistical effects such as varying injection rates of the nozzle might be a possible explanation here. Further measurements with the same experimental configuration might give more insight.

4.2.2 Nozzle Consumption at 20 bar backing pressure

In a subsequent experiment with the same experimental setup, the nozzle pressure was increased to around 20 bar with the HPS pressure starting at 100 bar. Fig.

4.8 shows the course of the LPS pressure during the course of the measurement.

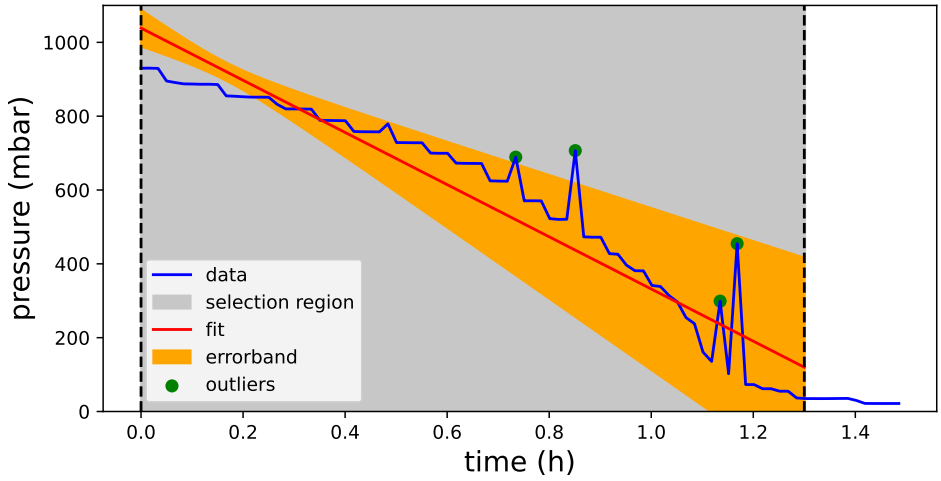

Figure 4.8: Pressure inside the LPS across time for a nozzle backing pressure of 20 bar. In contrast to the former measurement, the pressure decreases much more rapidly. The outliers have not been taken into account for fitting.

Apparently, the curve does not show the linear behaviour as the one depicted in Fig. 4.5, but a decrease can be seen nevertheless. In order to estimate the losses over time at the respective nozzle pressure, again, a linear function is fitted to the LPS pressure. To get a more accurate value for the loss rate, the outliers are not included for the fit, for the same reason as above. With a pressure decrease of $(-707 \pm 22)\,\mathrm{mbar/h}$, it is clear that gas is lost much more rapidly than before. Because the other compartments showed no measurable change in pressure this time, the amount of gas being ejected by the nozzle can be directly calculated by applying Eqn. 4.3. This leads to a total volume loss rate of $(-14.62 \pm 0.46)\,\mathrm{SL/h}$. Heuristically, we would expect a proportional relation between the pressure applied to the nozzle and the amount of gas flowing through, even though, this cannot be entirely correct, due to turbulences arising and non-linear effects that stem from the nozzle shape. However, it might be a good way to estimate the flow rate.
For this, the ratio of flow rates should match the ratio of nozzle backing pressure ($\dot{V}_{n,2}/\dot{V}_{n,1} = p_2/p_1$). In this case the ratios are

$$r_V = \frac{\dot{V}_{n,2}}{\dot{V}_{n,1}} = 2.525 \pm 0.079 \quad \text{and}$$
$$r_p = \frac{p_2}{p_1} = 2.3810 \pm 0.031 \ ,$$

which means we have a deviation of $1.7\,\sigma$, indicating a rough agreement on the estimate.

4.3 Recycling

Next, the efficiency of the system regarding the recycling of noble gases is examined. The system was filled with argon to the point where the HPS reached a pressure of 55 bar, the intermediary tank was at about 8 bar and the LPS approached atmospheric pressure. In total this corresponds to about 50 SL of argon inside the entire system. The nozzle pressure was set to 8.0 bar. In order to recycle all gas flowing through the nozzle, the valves above the TMP were set, such that the DIF1, DIF2, DIF3 and MAIN TMPs exhausts are all pumped by the same fore-vacuum pump. That way, all gas inside the main chamber that gets ejected by the TMPs is re-collected from the output of the big roots pump that is now used as the input for the LPS. This time, additionally to the digital recording of the LPS pressure, the data of a mass spectrometer connected to the main chamber was logged alongside with it.

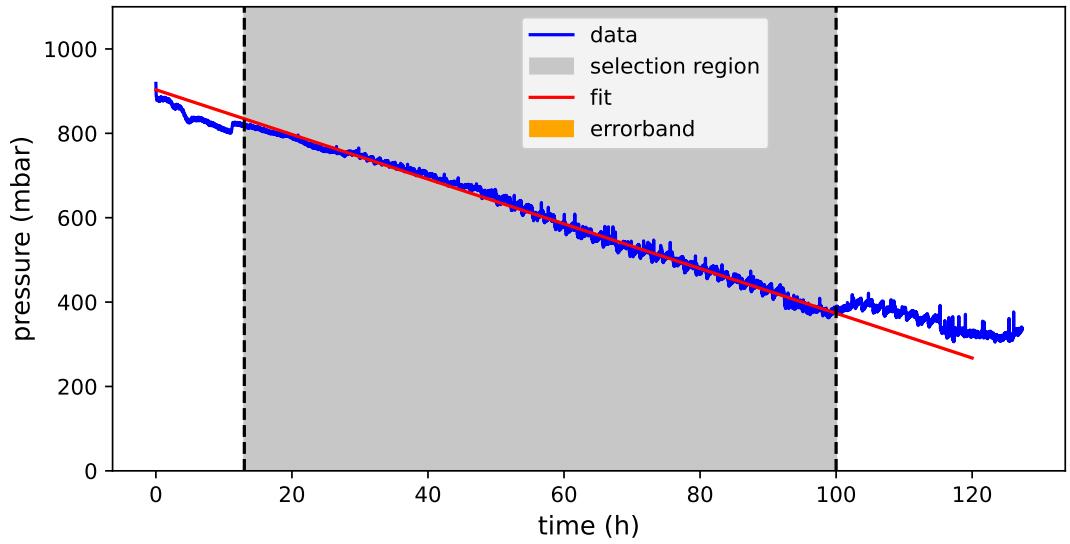

Figure 4.9: The pressure drop of the LPS is recorded over time and a linear function is fitted to extract the general trend. Since the uncertainties of the fit-parameters are small, the errorband is invisible.

As can be seen in Fig. 4.9, the pressure drops linearly, especially in the interval between 20 h and 100 h. From the fit, a decrease rate of (-5.299 ± 0.005) mbar/h can be obtained, which, combined with an offset ((903.4 ± 0.3) mbar) and the assumed inaccuracy of measurement of 10 mbar, gives a χ^2_{red} -sum of 0.97. This decrease rate corresponds to a loss of (0.1077 ± 0.0018) SL/h inside the LPS compartment. The HPS lost approximately (4 ± 1) bar over the the course of the entire measurement (127 h), which is equivalent to $(8.4 \pm 2.1) \times 10^{-3}$ SL/h.
The gas loss in the other compartments are negligible compared to the HPS and LPS. Again, the assumption that the other compartments stay roughly constant

in pressure as long as the LPS pressure does not approach 0, is verified.

With this configuration, theoretically, we would only need to add one liter of target gas every ten hours to keep the nozzle running at a backing pressure of 8 bar. This is a huge improvement considering that the nozzle consumption at a comparable nozzle pressure would be 5.8 SL/h without gas recycling. This translates to a loss (and therefore cost) reduction of over 98 %.

However, the issues rendering gas recycling complicated have to be considered here too. The biggest issue to be mentioned is the fact that the various parts of the recycling system are not entirely vacuum-tight leading to contamination from gases in the atmosphere surrounding the experiment. Once these gases enter the system, they should also be detectable by a mass spectrometer inside the main chamber, albeit in much smaller quantities.

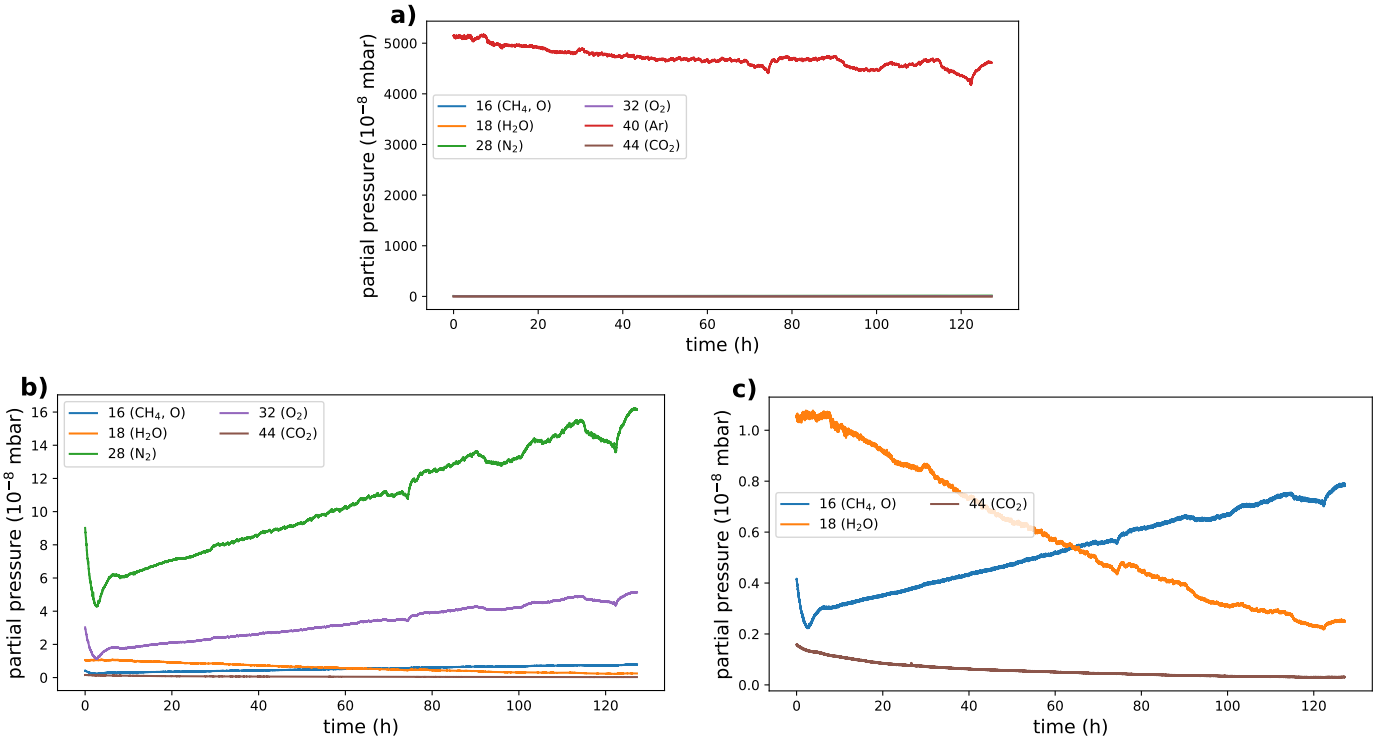

Figure 4.10: Partial pressures of the different substances entering the main chamber, sorted by their atom/molecule masses in u with according possible chemical compounds.

Fig. 4.10 shows the abundance of atoms/molecules with different masses over time. Since the mass spectrometer does not identify the kind of particle, but only its mass, all masses must be assigned a chemical species.
Tab. 4.2 shows a possible classification based on chemicals used in the experiment.

Table 4.2: Assignment of chemicals to the different masses detected in the mass spectrometer.

Mass (u)	Compound
16	CH_4, O
18	H_2O
28	N_2
32	O_2
40	Ar
44	CO_2

It should be noted here that there are principally more chemical combinations possible. The fact that argon was used as a proxy for future xenon gas to be recycled, suggests that the high abundance of atomic particles with a mass of 40 u inside the main chamber can largely be attributed to said argon.
Comparing the course of molecular nitrogen and oxygen, the similarity between the curves is immediately noticeable. With the roughly constant ratio of $p_{N_2}/p_{O_2} \approx 3.2$, the occurance of these two elements is attributed to contamination of the target gas with air flowing in from the outside. The earths atmosphere features a ratio in partial pressure of roughly 3.7. Interestingly, both curves exhibit a linear increase over time with the exception of the first hours of measurement. While the increase can be attributed to some small leaks in the LPS, the sharp drop in partial pressure in the beginning is probably due to some remaining air inside the nozzle part of the recycling system that was not flushed out before the measurement started, which was then exhausted by the TMPs right at the start. The level of increase shown by the nitrogen and oxygen curve might serve as an indicator of leakage rate of atmospheric contaminants in later measurements.

Fig. 4.10 (c) shows the partial pressures of some rarer substances, most notably water (H_2O) decreasing in abundance over time due to the installed water-filters. One rather mysterious part of the rarer gases found by the mass spectrometer is the one with a mass of 16 u. There are multiple possible compounds with this mass playing a role here. One possibility would be that somehow, methane (CH_4) entered the system. However, methane is not directly used in this experiment, and its natural abundance is by far smaller than a sixth of that of oxygen as suggested by the measured ratio here. Another explanation could be the presence of oxygen radicals (O) stemming from the decay of ozone (O_3) having the same mass as methane. Although ozone is used in the experiment in order to keep the mirrors clean, the flow into the chamber is only used during laser operation, which was not the case during this measurement. Possible residual traces of ozone can also be ruled out here, otherwise a high partial pressure of a substance with the mass of 48 u should be measurable, which was not found.
The fact that the shape of the curve regarding the compound with a mass of 16 u resembles that of nitrogen and oxygen so closely, combined with no plausible source

of other molecules with that specific mass, suggests another possibility: perhaps some of the molecular oxygen entering the main chamber got ionized and thus leading to the presence of some atomic oxygen.

The last significant measured molecule has a mass of 44 u. Although there are some organic compounds with this mass, such as acetaldehyde (CH_3CHO), the most reasonable assumption regarding the type of chemical is carbon dioxide (CO_2), since it is part of the atmosphere and emerges from many oxidation processes.

To show the influence of contamination over time, the ratio of all partial pressures except argon divided by the one of argon is shown in Fig. 4.11. The overall trend is remarkably similar to those of nitrogen and oxygen shown in Fig. 4.10 (b), since those two make up the biggest proportion of contaminants and because the partial pressure of argon stays roughly equal over time.

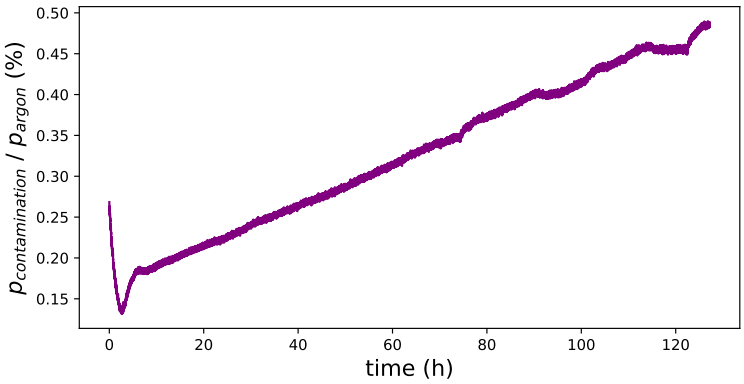

Figure 4.11: Ratio between contamination and target gas (argon). The overall trend of the curve is strongly dominated by the partial pressures of nitrogen and oxygen.

Perhaps the most intriguing feature of this curve is that it shows that the proportion of contaminants stays below 0.5 % across the entire duration of the measurement spanning over 120 hours, increasing only by a factor of 3 to 4.

5 Conclusion and Outlook

The recycling system characterized in this work was designed to reduce the demand for rare noble gases used as a target gas enabling high harmonics generation, the heart of the extreme-ultraviolet frequency comb. This device, small enough to be regarded as a tabletop experiment, makes precision spectroscopy of highly charged ions possible, allowing precision tests of fundamental physics in the future. The closed-loop recycling system starts with a differential pumping system consisting of three turbomolecular pumps placed directly above a nozzle set directly below a cavity focus injecting the target gas, followed by a fore-vacuum pump, various filters, tanks, a compressor station and a pressure regulator ensuring a constant nozzle backing pressure.

Measuring the pressures inside the different compartments was done with multiple kinds of pressure gauges, some for quantifying ultra-high vacuum conditions, others for up to 250 bar. Whilst the low-pressure gauges can be read out digitally, the other need a reliable means to determine the strength of a current output. For this purpose, a read-out system was constructed for logging the measured pressure of these gauges. However, due to delays in delivery of said devices, they were not employed until now.

An investigation of the nozzle flow with argon as a proxy gas indicated a consumption of about 5.8 SL/h for a nozzle backing pressure of 8.4 bar and 14.6 SL/h at 20 bar. With a cost of over 15 €/SL (xenon), these flow rates result in considerable monetary investments for prolonged periods of experiments relying on xenon as a target gas.
Employing full recycling using all turbomolecular pumps inside the main chamber of the experiment housing the cavity showed that the recycling system can reduce the effective consumption down to roughly 0.11 SL/h at a nozzle pressure of 8.4 bar, meaning 98 % of the previously dissipated gas can be saved. Concurrent monitoring with a mass spectrometer showed that the system used enabled gas recycling with a contamination ratio of less than 0.5 % after 120 hours corresponding to tripling of the contamination level at the start of the measurement.

With the possibility of recycling the rare gases needed for high harmonics generation as well as velocity map imaging, calibration of the parts sensitive to external perturbations and prolonged experiments requiring continuous nozzle flow can be carried out at much lower costs than previously.

With the utilization of high pressure gauges, more accurate measurements can be carried out, taking the conditions of the compartments housing gas with higher

pressure into account. Additionally, real time monitoring of the entire system will be possible.

With this, the gas recycling system was successfully tested and is now able to be put into operation for long-time measurements involving high-harmonic generation.

In further measurements, the behavior of the recycling system toward other kinds of gases could be analyzed. Helium and xenon have quite different properties when it comes to their tendency to diffuse through the walls of a metal container, so the type of gas used can have a strong influence on the efficiency of the system.

6 Acknowledgements

I want to thank J.-H. Oelmann, T. Heldt and L. Guth for their effort introducing me to the XUV project, their readiness to help me with questions regarding my thesis and just their overall support. A special thank you to J.R. Crespo López-Urrutia for starting my interest in the topic, for the detailed explanation of some fundamental (and sometimes less fundamental) questions of mine and for always believing in his students.

The quality of my time being here would not have been the same without the awesome people in the students office, which is why I also want to thank you for your friendliness, all the interesting (and sometimes off-topic) discussions and your dedication to plants making the bureau greener.

Finally, I want to thank everybody in this group for all the conversations, be it at EMBL´s canteen, your visits in the students office or at the Affenfelsen. Especially the last one should be highlighted here, for it was the location of so many awesome cake-gatherings, which was often the prime motivation of getting ahead.

A Bibliography

[1] Yuji Sano, Bernard Marty, and Pete Burnard. "Noble gases in the atmosphere". In: *The noble gases as geochemical tracers*. Springer, 2013, pp. 17–31.

[2] Herbert Baum, Torsten Geissler, and Ulrich Westerkamp. "Cost-benefit and break-even analysis of Xenon headlights in Germany and in EU-27". In: *Zeitschrift fur Verkehrswissenschaft* 80.2 (2009), p. 118.

[3] 2001. URL: https://www.esa.int/Applications/Telecommunications_Integrated_Applications/Ion_propulsion_system_to_the_rescue (visited on 05/07/2022).

[4] Shida Tan et al. "Nanomachining with a focused neon beam: A preliminary investigation for semiconductor circuit editing and failure analysis". In: *Journal of Vacuum Science & Technology B, Nanotechnology and Microelectronics: Materials, Processing, Measurement, and Phenomena* 29.6 (2011), 06F604.

[5] Thomas Marx et al. "Xenon anaesthesia". In: *Journal of the Royal Society of Medicine* 93.10 (2000), pp. 513–517.

[6] AD Shiner et al. "Probing collective multi-electron dynamics in xenon with high-harmonic spectroscopy". In: *Nature Physics* 7.6 (2011), pp. 464–467.

[7] E Constant et al. "Optimizing high harmonic generation in absorbing gases: Model and experiment". In: *Physical Review Letters* 82.8 (1999), p. 1668.

[8] Fritz Keilmann, Christoph Gohle, and Ronald Holzwarth. "Time-domain mid-infrared frequency-comb spectrometer". In: *Optics letters* 29.13 (2004), pp. 1542–1544.

[9] Andrew J Metcalf et al. "30 GHz electro-optic frequency comb spanning 300 THz in the near infrared and visible". In: *Optics Letters* 44.11 (2019), pp. 2673–2676.

[10] Ioachim Pupeza et al. "Extreme-ultraviolet frequency combs for precision metrology and attosecond science". In: *Nature Photonics* 15.3 (2021), pp. 175–186.

[11] Th Udem, Ronald Holzwarth, and Theodor W Hänsch. "Optical frequency metrology". In: *Nature* 416.6877 (2002), pp. 233–237.

[12] Neil Ashby. "Relativity in the global positioning system". In: *Living Reviews in relativity* 6.1 (2003), pp. 1–42.

[13] Paul Adrien Maurice Dirac. “The quantum theory of the electron”. In: *Proceedings of the Royal Society of London. Series A, Containing Papers of a Mathematical and Physical Character* 117.778 (1928), pp. 610–624.

[14] Edward W Kolb, Malcolm J Perry, and TP Walker. “Time variation of fundamental constants, primordial nucleosynthesis, and the size of extra dimensions”. In: *Physical Review D* 33.4 (1986), p. 869.

[15] JC Berengut and VV Flambaum. “Astronomical and laboratory searches for space-time variation of fundamental constants”. In: 264.1 (2011), p. 012010.

[16] Pacôme Delva and Jérôme Lodewyck. “Atomic clocks: new prospects in metrology and geodesy”. In: *arXiv preprint arXiv:1308.6766* (2013).

[17] Andrew D Ludlow et al. “Optical atomic clocks”. In: *Reviews of Modern Physics* 87.2 (2015), p. 637.

[18] Sigfrido Leschiutta. “The definition of the ‘atomic’second”. In: *Metrologia* 42.3 (2005), S10.

[19] Wolfgang Demtröder. *Experimentalphysik 3: Atome, Moleküle und Festkörper*. Springer-Verlag, 2010.

[20] Dominic Meiser et al. “Prospects for a millihertz-linewidth laser”. In: *Physical review letters* 102.16 (2009), p. 163601.

[21] Marc Eichhorn. *Laserphysik: Grundlagen und Anwendungen für Physiker, Maschinenbauer und Ingenieure*. Springer-Verlag, 2012.

[22] Steven T Cundiff. “Phase stabilization of ultrashort optical pulses”. In: *Journal of Physics D: Applied Physics* 35.8 (2002), R43.

[23] Janko Nauta. “An extreme-ultraviolet frequency comb enabling frequency metrology with highly charged ions”. PhD thesis. Ruprecht-Karls-Universität Heidelberg, 2020.

[24] F Quinlan et al. “Harmonically mode-locked semiconductor-based lasers as high repetition rate ultralow noise pulse train and optical frequency comb sources”. In: *Journal of Optics A: Pure and Applied Optics* 11.10 (2009), p. 103001.

[25] M Tsuzuki et al. “Midinfrared optical frequency comb based on difference frequency generation using high repetition rate Er-doped fiber laser with single wall carbon nanotube film”. In: *Photonics Research* 4.6 (2016), pp. 313–317.

[26] Paul B Corkum. “Plasma perspective on strong field multiphoton ionization”. In: *Physical review letters* 71.13 (1993), p. 1994.

[27] LV Keldysh et al. “Ionization in the field of a strong electromagnetic wave”. In: *Sov. Phys. JETP* 20.5 (1965), pp. 1307–1314.

[28] Zhifang Deng and Joseph H Eberly. “Multiphoton absorption above ionization threshold by atoms in strong laser fields”. In: *JOSA B* 2.3 (1985), pp. 486–493.

[29] Wolfgang Demtröder and Band Experimentalphysik. *Elektrizität und Optik*. Vol. 2. Springer, 2009.

[30] Jean-Claude Diels and Wolfgang Rudolph. *Ultrashort laser pulse phenomena*. Elsevier, 2006. ISBN: 9780122154935.

[31] Wolfgang Demtröder. *Experimentalphysik*. Vol. 4. Springer, 1998.

[32] Hans Dieter Baehr and Stephan Kabelac. *Thermodynamik*. Vol. 12. Springer, 1966.

[33] HJ Achtermann et al. “Precise determination of the compressibility factor of methane, nitrogen, and their mixtures from refractive index measurements”. In: *International Journal of Thermophysics* 7.3 (1986), pp. 709–720.

[34] J Nauta et al. “100 MHz frequency comb for low-intensity multi-photon studies: intra-cavity velocity-map imaging of xenon”. In: *Optics letters* 45.8 (2020), pp. 2156–2159.

[35] J Nauta et al. “XUV frequency comb production with an astigmatism-compensated enhancement cavity”. In: *Optics Express* 29.2 (2021), pp. 2624–2636.

[36] Lisa Schmöger et al. “Coulomb crystallization of highly charged ions”. In: *Science* 347.6227 (2015), pp. 1233–1236.

[37] Lisa Schmöger. “Kalte hochgeladene Ionen für Frequenzmetrologie”. PhD thesis. Ruprecht-Karls-Universität Heidelberg, 2017.

[38] Ronja Pappenberger. “Implementierung eines differentiellen Pumpsystems zur Erzeugung eines ultravioletten Frequenzkamms in einem optischen Resonator”. Cand. thesis. Ruprecht-Karls-Universität Heidelberg, 2019.

[39] J. Nauta. “A low-vibration, differentially pumped vacuum system for intracavity high-harmonic generation.” In: Max-Planck Insitut für Kernphysik. Saupfercheckweg 1, Heidelberg, Germany.

[40] Nick Lackmann. “Development of a Focusing Beamline for an Extreme-Ultraviolet Frequency Comb”. Cand. thesis. Ruprecht-Karls-Universität Heidelberg, 2021.

[41] BM Oliver, James G Bradley, and Harry Farrar IV. “Helium concentration in the Earth’s lower atmosphere”. In: *Geochimica et Cosmochimica Acta* 48.9 (1984), pp. 1759–1767.

Erklärung:

Ich versichere, dass ich diese Arbeit selbstständig verfasst habe und keine anderen als die angegebenen Quellen und Hilfsmittel benutzt habe.

Heidelberg, den 18.07.2022 .....